Applied Physics Reviews

AIP Publishing

REVIEW ARTICLE | MARCH 07 2023

High-pressure studies of atomically thin van der Waals materials

Special Collection: Quantum Materials and 2D superlattices

Luiz G. Pimenta Martins ; Riccardo Comin ; Matheus J. S. Matos ; Mário S. C. Mazzoni ; Bernardo R. A. Neves ; Matthew Yankowitz

Appl. Phys. Rev. 10, 011313 (2023)
https://doi.org/10.1063/5.0123283

Applied Physics Reviews REVIEW scitation.org/journal/are

High-pressure studies of atomically thin van der Waals materials

Cite as: Appl. Phys. Rev. **10**, 011313 (2023); doi: 10.1063/5.0123283
Submitted: 29 August 2022 · Accepted: 13 February 2023 ·
Published Online: 7 March 2023

Luiz G. **Pimenta Martins**,[1,a)] **Riccardo Comin**,[1,b)] **Matheus J. S. Matos**,[2,c)] **Mário S. C. Mazzoni**,[3,d)] **Bernardo R. A. Neves**,[3,e)] and **Matthew Yankowitz**[4,5,f)]

AFFILIATIONS

[1]Physics Department, Massachusetts Institute of Technology, Cambridge, Massachusetts 02139, USA
[2]Departamento de Física, Universidade Federal de Ouro Preto, Ouro Preto MG 35400-000, Brazil
[3]Departamento de Física, Universidade Federal de Minas Gerais, Belo Horizonte MG 31270-901, Brazil
[4]Department of Physics, University of Washington, Seattle, Washington 98195, USA
[5]Department of Materials Science and Engineering, University of Washington, Seattle, Washington 98195, USA

Note: This paper is part of the special collection on Quantum Materials and 2D superlattices.
[a)]**Author to whom correspondence should be addressed:** lmartins@mit.edu
[b)]**Electronic mail:** rcomin@mit.edu
[c)]**Electronic mail:** matheusmatos@ufop.edu.br
[d)]**Electronic mail:** mazzoni@fisica.ufmg.br
[e)]**Electronic mail:** bernardo@fisica.ufmg.br
[f)]**Electronic mail:** myank@uw.edu

ABSTRACT

Two-dimensional (2D) materials and their moiré superlattices represent a new frontier for quantum matter research due to the emergent properties associated with their reduced dimensionality and extreme tunability. The properties of these atomically thin van der Waals (vdW) materials have been extensively studied by tuning a number of external parameters such as temperature, electrostatic doping, magnetic field, and strain. However, so far pressure has been an under-explored tuning parameter in studies of these systems. The relative scarcity of high-pressure studies of atomically thin materials reflects the challenging nature of these experiments, but, concurrently, presents exciting opportunities for discovering a plethora of unexplored new phenomena. Here, we review ongoing efforts to study atomically thin vdW materials and heterostructures using a variety of high-pressure techniques, including diamond anvil cells, piston cylinder cells, and local scanning probes. We further address issues unique to 2D materials such as the influence of the substrate and the pressure medium and overview efforts to theoretically model the application of pressure in atomically thin materials.

TABLE OF CONTENTS

I. INTRODUCTION

Two-dimensional (2D) materials can be defined as materials with a thickness of one or a few atoms.[1] From the perspective of quantum matter research, the reduced dimensionality in 2D materials is linked to a reduction in the available phase space and the electronic screening of Coulomb forces, leading to enhanced quantum effects and increased interactions.[2] For this reason, 2D materials often exhibit outstanding transport, optical and magnetic properties that have been intensively investigated over the past decades.[3] The ability to stack dissimilar vdW crystals atop one another is another major advantage of these materials, forming the so-called van der Waals heterostructures featuring atomically sharp interfaces.[3] Lattice mismatches and/or twist angles between neighboring crystals further lead to the emergence of moiré patterns—geometric interference patterns that act as periodic potentials—which often result in a rich variety of physical phenomena not observed in the individual vdW layers alone. In order to glean insight into the physics of 2D vdW materials and moiré heterostructures and unlock new materials functionalities, the properties of these systems have been extensively studied by tuning various external parameters including temperature,[4–6] electric field,[7–9] electrostatic doping,[10–13] magnetic field,[14–16] and in-plane strain.[17–20] Pressure is another important thermodynamic variable that can be used to tune the properties of materials, serving to reduce interatomic distances, strengthening interatomic and magnetic interactions, and modifying the electronic density. Pressure, therefore, enables the realization of new physical phenomena as well as new material structures that are not accessible under ambient conditions. The relative scarcity of high-pressure studies involving 2D materials and heterostructures reveals that these are challenging experiments, but also present an opportunity to study a relatively untapped research field with a wealth of interesting new potential phenomena.

Contrasting to other review articles on high-pressure studies of 2D systems,[21,22] this review focuses solely on atomic-thin materials, which present their own experimental and theoretical challenges when compared to bulk 2D-layered van der Waals materials such as graphite (which sometimes are also referred to as 2D). For instance, it is well established that for atomically thin materials subjected to hydrostatic compression, the in-plane compression forces are exerted by the substrate via its adhesion to the 2D system, and not by the pressure medium, unlike for bulk materials.[23–25] Also, unlike bulk materials, different compressibility between a solid pressure medium and the substrate can lead to stress gradients that can significantly affect the interpretation of the experimental data. In this review, we address those issues in detail. Furthermore, previous reviews on the topic focused on high-pressure experiments using the diamond anvil cell (DAC) technique. In our work, apart from DACs, we review several high-pressure studies of atomically thin van der Waals materials using piston-cylinder cells and scanning probe microscopy techniques. An additional and important element of novelty is a dedicated session to the theoretical approach to model atomically thin systems at high pressures, including the theoretical formalism to simulate the application of pressure in those systems.

This review is arranged as follows: Secs. II–IV describe high-pressure studies performed using different experimental techniques: diamond anvil cells (DACs), piston-cylinder cells, and scanning probe microscopy, respectively. A description of the instrumentation of each technique is reviewed at the beginning of each section. Section V discusses the theoretical aspects of modeling atomic thin materials under compression. Section VI concludes with possible future research directions in this field.

II. HIGH-PRESSURE EXPERIMENTS WITH DIAMOND ANVIL CELLS

The field of high-pressure research has continuously expanded since the pioneering work of Percy W. Bridgman, who won the Nobel Prize in Physics in 1946 for the invention of an instrument to produce extremely high pressures, and for his discoveries within the field of high pressure physics.[26] In the Bridgman era (∼1910–1950), high-pressure experiments were performed using the so-called Bridgman anvil and piston cylinder devices, which allowed to perform electrical resistance and compressibility measurements up to 10 GPa,[27] (as a comparison, the pressure at Earth's core is estimated to be around 350 GPa). The diamond anvil cell (DAC) was later developed in 1958,[28] revolutionizing high-pressure research since it allowed direct optical observation of the effects of static pressure on matter through different experimental techniques such as x-ray diffraction, optical absorption, reflectivity, and Raman spectroscopy.[27] Nowadays, the typically accessible pressure achieved in DAC experiments ranges from 0.1 GPa to about 400 GPa- considered the pressure limit for conventional DACs[29]—however, improvements in DAC design can bring the maximum pressure to the terapascal range.[30] That range of pressures provides a platform to study fundamental physical phenomena, such as insulator–metal transitions,[31,32] classical phase transitions,[33,34] quantum phase transitions,[35,36] and high-temperature superconductivity.[37,38]

Furthermore, given that the rules of chemistry can be quite different at high pressures, several new exotic materials have been obtained from high-pressure experiments[39,40] such as materials with unprecedented stoichiometries[41] and with unusual chemical bonding.[42] Therefore, high-pressure studies using DACs constitute a powerful experimental technique in condensed matter physics to synthesize new materials, tune materials' properties, and observe novel many-body physics phenomena.

A. Instrumentation and experimental technique

1. DAC operation

Figure 1 shows schematics of a DAC. The principle of its operation is quite simple. One initially places a thin metallic disk—the gasket—with a pre-drilled hole, on top of the flat tip—the culet—of the bottom diamond. The dimensions of the gasket hole are typically 1/3–1/2 of the culet's diameter on the order of $\sim 10^2\,\mu$m. Then, one adds the sample and a manometer—usually a few ruby crystals—inside of the gasket hole, together with the pressure transmitting medium (PTM). By bringing the top diamond as shown in Fig. 1, the pressure chamber will be sealed, with the sample, the pressure indicator, and the PTM contained by the gasket walls and the two culets of the diamonds. High pressures are generated when the opposite diamonds are pushed together, squeezing the gasket and, therefore, the chamber, compressing the pressure medium, which transmits the forces to the sample. In this way, the uniaxial compression applied along the DAC axis is converted into hydrostatic pressure by the use of the PTM. However, the degree of hydrostaticity highly depends on the choice of the PTM as well as the sample/PTM volume ratio, as will be later discussed. Since the compressed area is quite small ($\sim 10^4$ $(\mu\text{m})^2$), large pressures can be generated with the application of moderate forces.

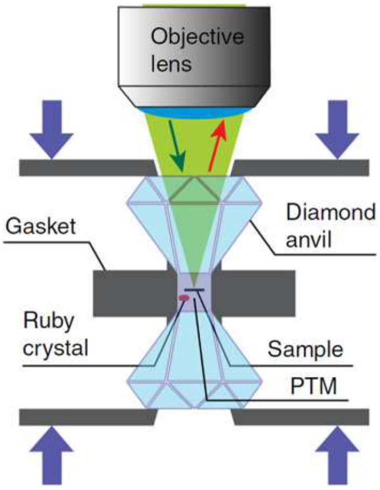

FIG. 1. Schematic of a diamond anvil cell. Cross section view of a DAC in which the sample is compressed hydrostatically when two opposite diamonds are pushed together, squeezing the gasket between them and compressing the pressure medium, which transmits the forces to the sample. Ruby crystals are usually used as the pressure indicators due to the pressure-induced shifts in their fluorescence energy. Reproduced with permission from Martins *et al.*, Nat. Commun. **8**, 1–9 (2017). Copyright 2017 Authors, licensed under a Creative Commons Attribution.

The pressure can be increased typically by tightening the screws that connect the two body parts of the DAC, with each body containing one diamond, or by the use of a membrane that can be inflated by the injection of an inert gas, which will push one body part against the other. Diamonds are chosen as anvils because of their superior hardness, being able to withstand pressures of GPa order without breaking, and the fact that they are transparent to x-rays and visible light. Thus, at each pressure, one can excite the system with a given light source, either a laser or a monochromatic x-ray beam, and collect the light emitted/scattered by the sample, therefore probing the modifications induced by pressure in the material. Different types of diamonds can be used, depending on the purpose. For instance, for Raman spectroscopy measurements, it is desirable to use diamonds with a very low defect density, typically type IIa diamonds, which will emit low-intensity fluorescence signals (originated from optical transitions between defect levels).

2. The gasket

The gasket is a crucial element for the operation of a diamond anvil cell. It (i) contains the PTM, allowing for the generation of hydrostatic pressures; (ii) prevents direct contact with the diamonds (since diamonds can break upon direct contact and applied force); and (iii) extrudes material around the diamonds, as illustrated in Fig. 1, forming a supporting ring which prevents the diamonds to crack due to the stress concentrated at the edges of the anvil faces.[27]

The gasket preparation usually starts with the indentation of the metal foil by squeezing it between the two anvils, which will reduce the thickness of the compressed area. Ideally one should use the same diamonds that will be used in the high-pressure experiment. The indentation is performed in order to minimize the plastic deformation during the experiment, such that only the necessary degree of thinning is applied in order to pressurize the PTM.[43] Typically the thinner the final indentation thickness is, the higher the maximum pressure will be.

After indentation, a hole is drilled at the center of the gasket with dimensions typically of 1/3–1/2 of the culet size, as previously mentioned, which will work as the pressure chamber. Then, for the experiment, it is important that the gasket is seated on the lower diamond in the same orientation as it had during the indentation so that the indentation marks can align with those from the diamond facets.

It is also important to choose the right material for the gasket for a given experiment. For instance, if the goal is to achieve higher pressures, one should choose hard yet malleable materials such as rhenium or stainless steel. It is also important to choose a material that is compatible with the PTM/sample for the experimental conditions. For instance, to avoid the formation of oxides originating from a chemical reaction between the PTM and the gasket material, stainless-steel gaskets are a suitable option.

3. Determining the pressure: The ruby fluorescence method

In high-pressure experiments using DACs, there are different methods that can be used to determine the pressure inside the chamber.[44–47] A widely popular method is ruby fluorescence.[44,45] In this method, small ruby crystals are inserted inside the gasket hole, as illustrated in Fig. 1, and are used as manometers.

The ruby crystals are composed of a Al_2O_3 matrix with Cr^{3+} impurities. Upon excitation with visible light, those crystals emit two fluorescence peaks termed as R_1 and R_2 at ambient temperature. The R_1 and R_2 lines are associated with electronic transitions within the Cr^{3+} impurity, and their energy will shift upon compression due to modifications in the crystal-field-split energy levels induced by pressure.[48] The calibration via ruby fluorescence is based on the evolution of the R_1-line energy with increasing pressure (P), and the connection between R_1 energy and P was established via concomitant x-ray diffraction measurements of four metals (Mo, Cu, Pd, and Ag) and the fitting of their specific volume with well-established equations of state for those metals.[44,45] Therefore, one can determine the pressure (in GPa units) via the shift in the R_1 line from ambient pressure conditions $\Delta\lambda = (\lambda(P) - \lambda(P_0))$, via the expression,

$$P[\mathrm{GPa}] = \frac{A}{B}\left[\left(1+\frac{\Delta\lambda[\mathrm{nm}]}{\lambda_0}\right)^{B} - 1\right], \qquad (1)$$

where the A and B constants are 1904 and 7665, respectively, and $\lambda_0 = 694,2$ nm is the wavelength of the R_1 fluorescence line at a pressure of 1 bar.[45]

Importantly, the positions of the R_1 and R_2 peaks also shift with temperature, and several works have investigated the pressure calibration both in the low-temperature[49] and high-temperature range.[50] Alternative methods to determine the pressure inside of the chamber in DAC experiments are: keeping track of the first-order Raman peak from the diamond window, which shows a linear shift with pressure,[46] or measuring the pressure-dependence of the specific volume of a reference material that has a well established-equation of state,[47] such as Ag and Cu, via high-pressure x-ray diffraction.

4. The choice of the pressure transmitting medium

Ideally, high-pressure experiments should be performed under hydrostatic conditions. However, every PTM solidifies after a given pressure, and upon solidification, the medium and consequently the sample can develop pressure gradients and local anisotropic stress components (also termed deviatoric stress) that can significantly affect the interpretation of the experimental data depending on their magnitude. A recent example is of the superconductor $CaFe_2 2As_2$ in which different high-pressure experiments reported conflicting conclusions about its PT phase diagram, with the contradiction being solved by the realization that the superconducting phase is extremely sensitive to non-hydrostatic conditions, being favored by uniaxial components while absent under hydrostatic conditions.[51] Therefore, it is extremely important to identify the hydrostatic limits of the PTM for a given HP experiment, as well as the presence and strength of pressure gradients and local non-hydrostatic stress components.

In order to quantify the degree of hydrostaticity of a given PTM, a very popular technique was introduced by the seminal work of Piermarini *et al.*[52] In their work, they investigated the hydrostatic limit of several PTMs in DAC experiments using two methods: (i) by measuring the pressure at several different locations from tiny ruby crystals spread across the chamber—which can give information about the presence of pressure gradients inside of the chamber, and (ii) by measuring the spectral linewidth of the R_1 fluorescence peak from ruby, which can give information about the presence of local non-hydrostatic stress components. The R_1 peak will broaden under the presence of local non-hydrostatic stress components because it is associated with an electronic transition within the Cr^{3+} impurities, which is highly sensitive to the local environment around the chromium ion.

This method remains popular and has still been used for instance, to determine the hydrostatic limits of several PTMs for low-temperature experiments,[53] in which the solidification of the PTM is unavoidable even at low pressures, due to the temperature drop. Importantly, some mediums can remain good quasi-hydrostatic PTMs even after their solidification, if the presence of deviatoric stress is sufficiently small. One example is the water PTM. Even though water solidifies at $\approx$1 GPa[54] at ambient temperature, previous studies[52,54,55] show a lack of evidence of significant pressure gradients or local non-hydrostatic stress components in the water medium up to approximately 8 GPa.

Table I shows the solidification pressure and quasi-hydrostatic limit at ambient temperature for several PTMs commonly used in high-pressure experiments.

Another important factor to take into account when analyzing the degree of hydrostaticity in an HP experiment is the sample/PTM volume ratio. The higher this ratio is, the lower the degree of hydrostaticity will be. Other relevant aspect of choosing a PTM is the difficulty of its loading process into the DAC. Liquid PTMs are fairly simple to load, as long as they are not volatile, whereas loading gases is considerably more difficult, often requiring equipment specifically designed for this purpose.

B. The influence of the substrate and the PTM: Strain transfer, sample detachment, and detection of stress gradients

One of the main differences between high-pressure experiments involving bulk vs atomically thin materials is the influence of the substrate and the PTM on their mechanical responses. While for bulk materials, the compression is directly exerted by the PTM, for atomically thin materials, it has been established that the in-plane compression is exerted by the strain transfer from the substrate via its adhesion to the 2D material.[23–25] That is, for a perfect adhesion, the extent to which the 2D material will be in-plane compressed will solely be

TABLE I. Solidification pressure and hydrostatic/quasi-hydrostatic range for several PTMs commonly used in high pressure experiments.

PTM	Solidification pressure at room temperature (GPa)	Hydrostatic/ quasi-hydrostatic range (GPa)	References
Water	1.0	~8.0	52, 54–56.
4:1 methanol/ ethanol	10.5	~10.5	57
Neon	4.8	~15	57
Helium	12.1	>40	57
Argon	1.4	~10	57
Nitrogen	2.4	~12.0	57

determined by the compressibility of the substrate. If the adhesion is not ideal, the mechanical response of the 2D material will be determined by the strain transfer from the substrate, while if the sample detaches from the substrate or if it is unsupported, its in-plane compression will be determined by the compressibility of the 2D material itself.[24,58] The influence of the PTM should particularly be taken into account once the PTM solidifies since eventual differential compressibility between the solid PTM and the substrate could lead to shear in-plane components on the 2D material[25] that could lead to lattice distortions and defects. In that context, Raman spectroscopy can provide direct information about the presence of stress/strain gradients across the compressed sample.[56,59] It was also initially proposed that the PTM could chemically dope the 2D samples upon compression,[60] which was later disproved[24] for the graphene case. This section describes these works.

Several groups have investigated the contributions from the substrate and the PTM in high-pressure DAC experiments via Raman spectroscopy by analyzing the pressure the evolution of the G band in graphene.[23–25] The G band (approximately at 1580 cm^{-1}) is associated with the in-plane C–C bond-stretching mode in the graphene lattice and is extremely sensitive to the effects of strain and also doping.[61] An important parameter to investigate the pressure evolution of Raman frequencies under strain is the Grüneisen parameter λ. For a quasi-harmonic mode ν of frequency ω_ν, the Grüneisen parameter λ_ν can be defined as[62]

$$\frac{\omega(P)}{\omega(P_0)} = \left(\frac{V(P)}{V(P_0)}\right)^{-\lambda_\nu}, \tag{2}$$

where P_0 is the initial pressure. In the graphite case, given the considerable anisotropy between in-plane and out-of-plane compressibilities, one can define the Grüneisen parameter for the G band considering only the in-plane compressibility[23] such that Eq. (2) can be rewritten as

$$\frac{\omega(P)}{\omega(P_0)} = \left(\frac{a(P)}{a(P_0)}\right)^{-2\lambda_G}, \tag{3}$$

where a is the lattice parameter of graphene.[23] From Eq. (3), one can see that the G band frequency (ω_G) will blueshift upon compression.

The first high-pressure work on graphene was carried out by Proctor *et al.*[23] In their work, the authors compressed and exfoliated few layer graphene samples on a 300-nm SiO_2-coated silicon substrate. For the mono, bi, and few-layer flakes on the SiO_2/Si substrate, they noticed that the thinner the sample is, the steeper its G band pressure slope ($d\omega_G/dP$) is, as shown in Fig. 2(a). They proposed that the thinner the sample is, the greater the influence of the substrate will be on its in-plane compression. Since the SiO_2/Si substrate is more compressible than graphene, $d\omega_G/dP$ will be higher for graphene on SiO_2/Si compared to unsupported graphene, the latter having similar $d\omega_G/dP$ to graphite. To quantify this effect, the authors plotted the pressure evolution of the G band using Eq. (3) considering silicon's compressibility for the $a(P)/a(P_0)$ term and graphene's Grüneisen parameter $\lambda_G = 1.99$ obtained from Ref. 63 [Fig. 2(b)]. For the G band, the agreement with the experimental data was good at low pressures (0–1.5 GPa) and started to deviate at higher pressures. The authors attributed the deviation to graphene debonding at higher pressures. In fact, we point out that the debonding could be due to the solidification of the N_2 PTM above 1.2 GPa, consistent with the results from the following work by Filintoglou *et al.*[24] The effect of the number of graphene layers and the adhesion to the SiO_2 substrate was studied in a subsequent work by Nicolle *et al.*[60] via a calculation that took into account the competition between the adhesion and the elastic energies for graphene to conform to the rough SiO_2 substrate. Their results showed that a debonding from the SiO_2 substrate occurs for graphene layer thickness above two, which should result in a $d\omega_G/dP$ slope similar to that of graphite. In the same work, the authors also proposed a giant doping effect from the PTM on their samples, which was later contested by Filintoglou *et al.*[24]

Filintoglou *et al.*[24] investigated the contributions of both substrate and PTMs on the pressure response of graphene. The authors compressed monolayer graphene samples grown by chemical vapor deposition (CVD) on copper substrates using a polar (4:1 methanol/ethanol, termed as alcohol by the authors) and non-polar (fluorinert) PTM. In the 0–3 GPa range, they observed that the pressure slope for the G band is the same for both PTMs, suggesting that the pressure response of the G band frequency is mainly dictated by mechanical stress rather than the pressure doping from the PTM. To further support this claim and disentangle, the contributions from doping and strain, the authors plotted the frequencies of the G and 2D band (ω_{2D}) at increasing pressures, following the work of Lee *et al.*[64] Their data show that the [ω_G(P), ω_{2D}(P)] points fall into a pure-strain line ($d\omega_{2D}$ $d\omega_G$ slope of 2.2 according to Lee *et al.*[64]) and constant electron-doping [Fig. 2(c)], confirming that the PTM does not significantly dope the samples as pressure increases. Importantly, the authors noticed a sudden drop in the frequency of the G band followed by an irreversible decrease in pressure slope from 9 cm^{-1}/GPa to 5.6 cm^{-1}/GPa around 2 GPa for the fluorinert PTM [Fig. 2(d)] without a significant broadening of the G bandwidth. They attributed this behavior to the fact that the PTM solidifies around that pressure, resulting in graphene being compressed between two solid surfaces, therefore, not being preferably adhered to the copper substrate, which should resemble the mechanical behavior of free-standing graphene. In fact, the pressure slope of 5.6 cm^{-1}/GPa is consistent with the recently reported slope of 5.4 cm^{-1}/GPa for unsupported graphene.[58]

In the light of the analysis by Filintoglou *et al.*,[24] an important issue to be analyzed is how differences in the compressibility between the PTMs, once it solidifies, and the substrate, can affect the mechanical response of a 2D material. This issue was investigated by Machon *et al.*[25] In their work, the authors analyzed bi-layer graphene samples on SiO_2/Si substrates compressed up to 8–10 GPa using three different PTMs:4:1 methanol/ethanol, water, and argon. Importantly, the 4:1 methanol/ethanol PTM remains liquid/hydrostatic up to 10.5 GPa, while water turns into Ice VI and Ice VII at approximately 1 and 2 GPa, respectively, and argon solidifies at 1.4 GPa- however, both water and argon PTMs remain quasi-hydrostatic up to higher pressures (see Table I). The authors observed a linear evolution of the G band frequency with pressure up to approximately 8 GPa for both the 4:1 methanol/ethanol and water PTMs, whereas the slope deviates from the linear behavior after the solidification pressure for the argon PTM [Fig. 2(e)]. To understand those results, the authors plotted the pressure evolution of the solid surfaces and their pressure derivatives for water, N_2, Ar, and SiO_2, shown in Fig. 2(f). Notice that the surface compressibility of water and SiO_2 are remarkably similar in the 0–8 GPa pressure range, resulting in an absence of in-plane shear

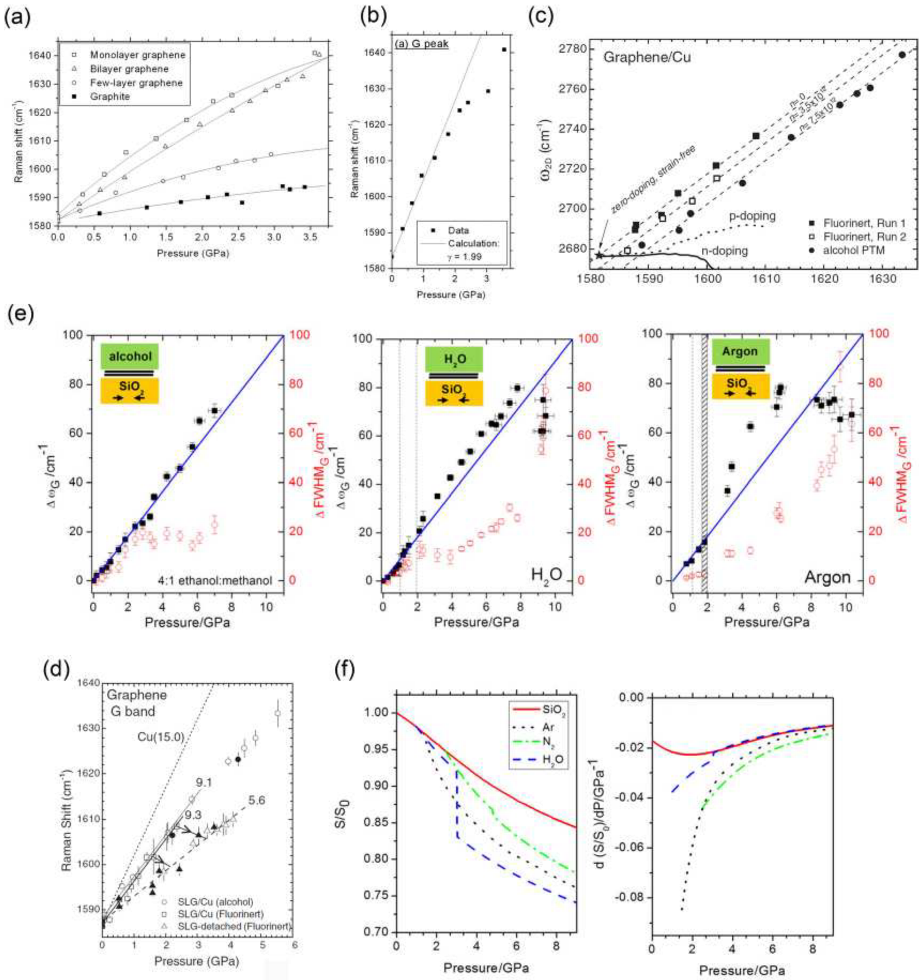

FIG. 2. Influence of the substrate and the PTM via analysis of the pressure-evolution of the Raman G band in graphene. (a) Raman frequencies of the G band as a function of pressure for mono-, bi, and few-layer graphene on a SiO_2-coated silicon substrate and of unsupported graphite using a N_2 PTM. (b) G band frequencies as a function of pressure for monolayer graphene on SiO_2/Si. The black solid line is the calculated ω_G using Eq. (3) considering silicon's compressibility $a(P)/a(P_0)$ and using a Grüneisen parameter of $\lambda_G = 1.99$ obtained from Ref. 63. [(a) and (b)] Reprinted with permission from Proctor *et al.*, Phys. Rev. B **80**, 073408 (2009). Copyright 2009 the American Physical Society. (c) Correlation between the Raman frequencies of the G (ω_G) and 2D (ω_{2D}) bands for monolayer graphene at increasing pressures to extract information about doping and strain. The filled and empty squares correspond to two different pressure runs using a flurorinert PTM, while the filled circles correspond to a pressure run using 4:1 methanol/ethanol PTM. The dotted straight lines correspond to pure-strain lines (constant doping) (d ω_{2D}/dω_G slope of 2.2[64]) (d). The star represents the (ω_{2D},ω_G) values for undoped, unstrained monolayer graphene obtained from Ref. 64. The solid and doted lines starting from the star symbol correspond to pure electron and hole doping (no strain), respectively, as obtained from Ref. 65. (d) Pressure evolution of the G band frequency for monolayer graphene on the copper substrate. Empty and filled symbols correspond to increasing and decreasing pressures. The circle and square symbols correspond to compression with alcohol and fulorinert PTMs, respectively, while the triangle symbol corresponds to compression with fluorinert after sample detachment. The dotted line is the calculated ω_G shift, considering the bulk modulus of copper and perfect adhesion of graphene. The numbers represent the dω_G/dP pressure slopes. [(c) and (d)] Reprinted with permission from Filintoglou *et al.*, Phys. Rev. B **88**, 045418 (2013). Copyright 2013 the American Physical Society. (e) G band frequency (black filled squares) and full width at half maximum (red empty squares) subtracted from their values at ambient pressure for bi-layer graphene on SiO_2/Si as a function of pressure for 4:1 methanol/ethanol (left panel), water (center panel), and argon (right panel) PTMs. The vertical dotted lines correspond to different pressure-induced phase transitions of the PTMs to a solid phase, while the hatched region for argon corresponds to its pressure recrystallization domain. (f) Surface compression (let panel) and its derivative (right panel) as a function of pressure for different PTMs. [(e) and (f)] Reproduced with permission from Machon *et al.*, J. Raman Spectrosc. **49** 121 (2018). Copyright 2018 John Wiley and Sons.

stress components, explaining the well-behaved linear evolution of G band frequency for the water case. On the other hand, the surface compressibility of solid Ar and SiO_2 are considerably different, introducing in-plane non-hydrostatic stress components, which would explain the deviations from the linear behavior of $d\omega_G/dP$.

We point out that a simple and direct method to determine the presence of pressure gradients generated by the PTM and/or substrate in an atomic-thin material is to acquire the Raman spectra at different locations across the sample. In the absence of considerably doping from the PTM (or if the doping can be considered to be homogeneous), significant variations in the Raman frequencies at different locations can be attributed to stress gradients. Using this method, Pimenta Martins *et al.*[56] measured ω_G at three different locations in graphene powder compressed using water as the PTM. The powder consisted of a mixture of graphene flakes with thicknesses ranging from mono-layer to graphite, with the majority of flakes (86% in mass) with thickness below 20 layers. For each pressure, the authors calculated the difference between the maximum and the minimum values ω_G values ($\delta\ \omega_G$). They observed that above 8 GPa, the $\delta\ \omega_G$ values start to increase, being a direct indication of the presence of pressure gradients, in qualitative agreement with the detection of pressure gradients in compressed water found by Piermarini *et al.*[52] This method was also used by Pimenta Martins *et al.*,[59] where the authors measured the Raman spectra of monolayer MoS_2 compressed in a 4:1 methanol/ethanol PTM at 4.5 GPa and 10 K (the PTM is solid at that temperature). The authors observed no deviations of all Raman peaks under these conditions, in qualitative agreement with the absence of deviatoric stress for the 4:1 methanol/ethanol PTM at low temperatures (5 and 77 K) at that pressure, as investigated by Tateiwa and Haga[53] and Feng *et al.*[66]

From the combined information from those previous works, one can infer that whenever the compressed 2D material is under good hydrostatic or quasi-hydrostatic conditions, the Raman frequencies will shift linearly, without a significant broadening of the peaks or changes in the Raman frequencies when measured at different locations at a given pressure.

To conclude this section, we highlight the recent work of Sun *et al.*,[58] which investigated the mechanical response of unsupported graphene samples in an N,N-dimethylformamide (DMF) PTM at high pressures. They argued that it is physically meaningful to attribute a c_{33} elastic constant to graphene, that is, monolayer graphene gets squeezed upon out-of-plane compression as a result of the compression of the out-of-plane p_z orbitals. Their conclusions were based on the analysis of the sub-linear evolution of the G band in unsupported graphene, which in analogy to the graphite case, can give information about the graphene's out-of-plane stiffness.

C. Evidence of pressure-induced formation of the 2D diamond from few-layer graphene

The isolation of graphene from the mechanical exfoliation of graphite[67] motivated the search for 2D-versions of selected bulk materials, since the reduced dimensionality could lead to novel and exotic properties, adding to those from their bulk counterparts. Diamond exhibits outstanding properties such as superior hardness and stiffness as well as the highest thermal conductivity at room temperature for bulk materials, apart from being transparent and chemically inert.[68] Therefore, experimental efforts have been directed toward obtaining an atomically thin diamond that could show additional unique features due to the quantum confinement. Several theoretical models have predicted 2D diamond structures with different properties, however, synthesizing stable and functional forms of these materials remains a current challenge. Different methods have been explored for its synthesis, including pressure-less chemical functionalization of bilayer graphene[69–71] as well as high-pressure compression of few-layer graphene using scanning probe microscopy tips[72–75] or hydrostatic compression using DACs.[56,76–78] This section focuses on the latter experimental method, while Sec. V B discusses different theoretical models of 2D-diamond structures. For a detailed review of all the experimental methods for 2D diamond synthesis, we refer the readers to Refs. 68 and 79.

The conversion of graphite to the cubic diamond at high pressures and high temperatures is a canonical example of the use of pressure to synthesize novel materials and constitutes a common route of diamond production for practical applications. However, previous high-pressure studies carried out with graphite at room-temperature showed evidence of a structural phase transition to an insulating, transparent, and sp^3 containing phase,[33,80–82] with several proposed crystal structures.[33,83–86] Similarly, recent DAC experiments carried out with few-layer graphene have obtained different evidence of a phase transition to a 2D-diamond like phase, with different structures being proposed.

The first experimental evidence for the existence of 2D diamond via hydrostatic compression was carried out by Pimenta Martins *et al.*[76] In their work, the authors compressed two layers of CVD graphene transferred onto a Teflon substrate using water as the PTM and they observed a phase transition to a 2D diamond-like phase using Raman spectroscopy. This technique was chosen due to its sensitivity to different atomic hybridizations in carbon materials.[87] Upon conversion of few-layer graphene to 2D diamond, as well as from graphite to bulk diamond, the carbon atoms change their hybridization from sp^2 to sp^3. The phase transition was detected by measuring the difference in frequency of the G band in the double-layer graphene system using two different laser excitation energies: 2.33 eV (green) and 2.54 eV (blue) ($\Delta\omega_G = \omega_{G,\text{blue}} - \omega_{G,\text{green}}$), as a function of pressure. According to Ferrari and Robertson.,[87] for a pure sp^2 system, one should expect that $\Delta\omega_G = 0$, whereas for a mixed sp^2–sp^3 system, $\Delta\omega_G \neq 0$ (more precisely, the G band frequency should increase by increasing the laser excitation energy[87]) Thus, by plotting $\Delta\omega_G$ as a function of pressure [see Fig. 3(a)], a clear discontinuity in $\Delta\omega_G$ can be seen at approximately 5 and 7.5 GPa for two different pressure runs, which can be associated with a structural sp^2 to sp^2–sp^3 phase transition. According to the authors, upon phase transition, an sp^3 matrix is formed, containing nanometer-sized sp^2 clusters. Importantly, the behavior of $\Delta\omega_G$ vs pressure cannot be affected by the solid PTM (water becomes Ice VI at 1 GPa and Ice VII at 2 GPa) since the Raman spectra using the 2.33 and 2.54 eV excitations were acquired at the same locations on the sample at each pressure. Furthermore, the authors found no evidence of phase transition (no significant change in $\Delta\omega_G$) up to 13 GPa for monolayer graphene compressed in water as well as for double-layer graphene compressed in mineral-oil PTM [Fig. 3(b)]. The latter results indicate that for the phase transition to occur, it is necessary at least two layers of graphene in the presence of water, in agreement with previous experimental results from tip-compression of few-layer graphene from Barboza

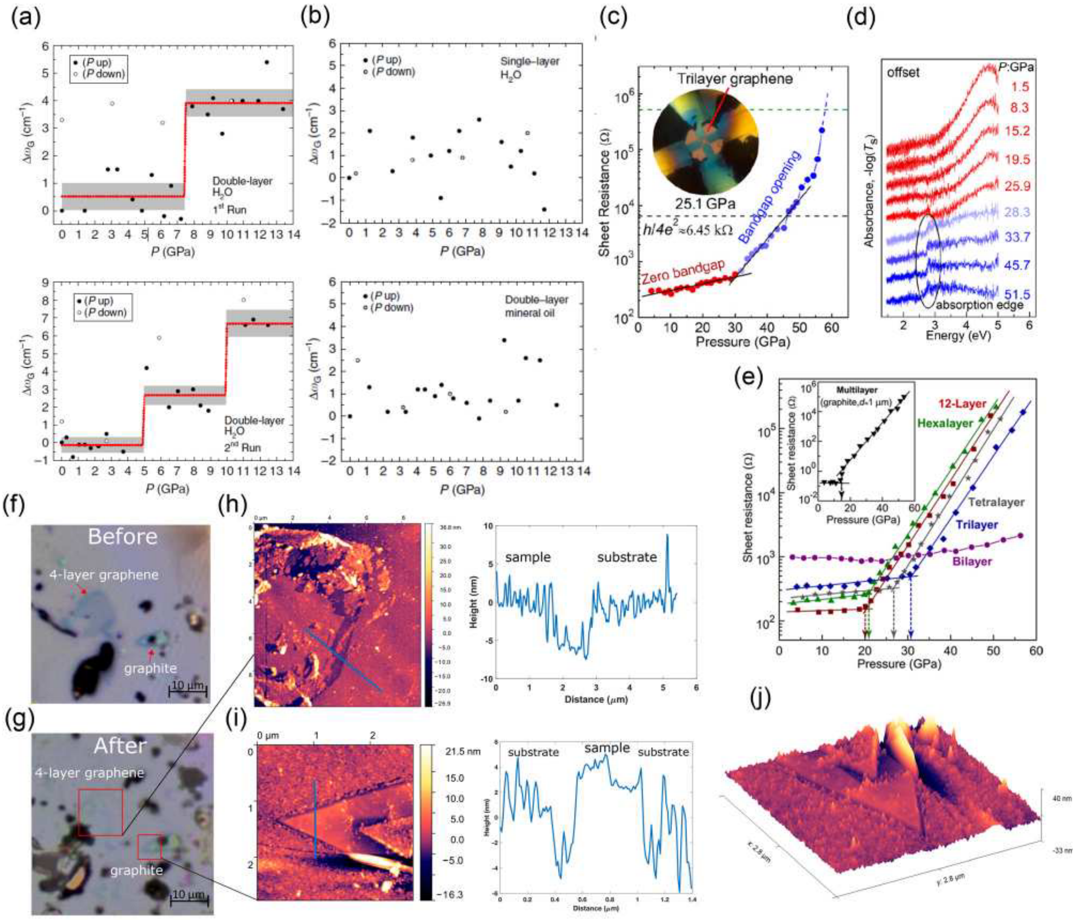

FIG. 3. Evidence of 2D diamond formation from high-pressure hydrostatic compression of few-layer graphene. (a) Pressure evolution of $\Delta\omega_G$, defined as the difference in the G band frequency measured with 2.54 and 2.33 eV excitation, for two different pressure runs of CVD double-layer graphene samples on a Teflon substrate compressed in a water PTM. (b) Pressure evolution of $\Delta\omega_G$ for monolayer graphene on Teflon compressed in water (top panel) and double-layer graphene on Teflon compressed in a mineral oil PTM. [(a) and (b)] Reproduced with permission from Martins *et al.*, Nat. Commun. **8** 1–9 (2017). Copyright 2017 Authors, licensed under a Creative Commons Attribution. (c) and (d) Sheet resistance (c) and optical absorbance measurements as a function of pressure for an exfoliated tri-layer graphene sample directly transferred onto the diamond culet. The ellipse in (d) highlights the presence of a weak absorption edge above approximately 30 GPa. [(c) and (d)] Reproduced with permission from Ke *et al.*, Proc. Natl. Acad. Sci. U. S. A. **116**, 9186 (2019). Copyright 2019 APS. (e) Sheet resistance as a function of pressure for exfoliated bi-, tri-, tetra-, hexa-, and 12-layer graphene samples directly transferred onto the diamond culet. Reprinted with permission from Ke *et al.*, Nano Lett. **20**, 5916–5921 (2020). Copyright 2020 American Chemical Society. (f)–(j) Evidence for the formation of a hard 2D phase for few-layer graphene compressed in water up to 8 GPa. (f)–(g) Optical images of a sample containing a four-layer graphene and a thin graphite flake on a SiO_2/Si substrate before (f) and after compression up to 8 GPa in water PTM (g). The red boxes indicate the regions of those sample where AFM measurements were carried out. (h)–(i) Topographical AFM images of the four-layer (h) and graphite (i) flakes where the blue lines correspond to height profiles shown on the on the right panels. Notice that samples and the substrate are leveled—an evidence for indentation. (j) Three-dimensional topographical AFM image of the graphite flake showing that it penetrated into the harder SiO_2/Si substrate. [(f)–(j)] Reprinted with permission from Pimenta Martins *et al.*, Carbon **173**, 744–747 (2021). Copyright 2021 Elsevier.

et al.[72] and with density functional theory calculations in these two works.[72,76] According to these calculations, the resulting structure is diamondene: a 2D ferromagnetic semiconductor with spin-polarized bands. Importantly, in diamondene, the chemical functionalization occurs only at the top graphene layer, leaving half the carbon atoms at the bottom layer with a dangling bond, which is responsible for the magnetism and spin-polarization properties.

The role of water is to provide the chemical species –H or –OH that will form covalent bonds with the top graphene layer at high pressures,[56,72,76] facilitating and stabilizing the sp^3 conversion. The exact mechanism for this chemical reaction remains elusive, but it is known that the reactivity of water molecules increases with pressure- for instance, the ionization constant of water increases by 100 from 0.1 MPa to 1 GPa.[88,89] In fact, Vasu *et al.*[89] reported on the synthesis of 2D structures of metal oxides by trapping their corresponding salts with water between graphene sheets. According to the authors, the pressure exerted by the van der Waals forces between the graphene sheets, which could be as high as 1 GPa, ionizes the trapped water and initiates the reaction that gives rise to the 2D sheets of metal oxides.

However, evidence of 2D diamond formation from compression of few-layer graphene has been reported even in the absence of chemical functionalization. Ke *et al.*[77] compressed an exfoliated tri-layer graphene sample using Daphne 7373 oil or argon PTMs (both chemically inert) and observed a bandgap opening at approximately 30 GPa via electrical and optical absorption measurements. For the transport measurements, the tri-layer graphene sample was transferred onto the diamond culet and the electrodes were directly patterned and deposited on top of it. The phase transition from a semi-metal to semiconductor was detected by monitoring the sheet resistance as a function of pressure and noticing a sudden increase in resistance at 33 GPa, followed by an increase by more than three orders of magnitude upon further compression to 59 GPa, as can be seen in Fig. 3(c). The sheet resistance showed a weak temperature-dependence below 34 GPa, significantly increasing with decreasing temperature above that pressure—a signature of semiconducting behavior. A bandgap of 2.5 eV was confirmed by UV-vis absorption measurements as shown in Fig. 3(d), highlighting the absorption edge. The authors proposed that this phase transition could be associated with a diamond-like 2D phase. Using the same experimental methodology, Ke *et al.*[78] compressed tri-, tetra-, hexa, and 12-layer graphene and from electrical resistance measurements, they observed a bandgap opening at 33.0, 27.1, 21.3, and 19.6 GPa, respectively [Fig. 3(e)]. Notice that as the number of graphene layers increases, the critical pressure decreases. From optical absorption measurements, all samples showed an absorption edge at approximately 2.8 eV. The authors proposed via DFT calculations that the new phase consists of an atomically thin hexagonal diamond, formed with no need of chemical functionalization. High-pressure x-ray diffraction (XRD) data from a graphene powder was provided to indicate the formation of a powder of hexagonal 2D diamonds; however, it is important to point out that their XRD signal could have contributions from thick graphite flakes that are usually present in graphene powders[90] or bulk-like structures formed from the interlayer bonding of several flakes.

The works thus far described in this section revealed isolated properties expected from a 2D diamond, such as sp^3 content,[76] transparency,[77] and superior hardness[73] (in this latter work, the compression was applied using an AFM tip, as discussed in Sec. IV B), providing different pieces for the 2D-diamond puzzle. However, to form a coherent picture and obtain robust evidence of its existence, one needs to probe these different properties in the same system under compression. Pimenta Martins *et al.*[56] performed such measurements, obtaining experimental evidence for the formation of a sp^3-containing, transparent and hard 2D phase by compressing few-layer graphene on a SiO_2/Si substrate using water as the PTM. Raman spectroscopy provided evidence of a phase transition from a sp^2 to a phase containing sp^2 and sp^3 domains at approximately 6 GPa for bi-layer graphene and starting at 4 GPa and ending at 7 GPa for five-layer graphene and graphite. For all these flakes, the evidence for the presence of sp^3 carbon came from an abrupt broadening of the G bandwidth, considered a signature of the presence of sp^3 carbon in compressed graphitic systems,[80,91,92] accompanied by a suppression of the 2D band intensity. Other sources of G band broadening such as due to inhomogeneous stress introduced by the PTM or to the differential compressibility between the solid PTM and the substrate were ruled out due to the lack of significant deviatoric stress for the water PTM up to approximately 8 GPa[52] (see discussion in Sec. II A 4) and the similarity between the surface compressibility of water (Ice VII) and the SiO_2 substrate[25] (see discussion in Sec. II B). The evidence of phase transition based on the suppression of the 2D band can be understood as follows. The 2D band (2 700 cm^{-1} under ambient conditions) arises from two-phonon double resonance Raman processes and can be drastically suppressed upon changes in the electronic structure caused by structural modifications in the graphene lattice.[93]

For the five-layer graphene and graphite flakes, an additional evidence of phase transition was a change in the ω_G vs P slope, becoming steeper between 4 and 7 GPa when compared to the 0–4 GPa range. As discussed in Sec. II B, a change in $d\,\omega_G/dP$ had been previously attributed to sample detachment by Filintoglou *et al.*, however in their work, $d\,\omega_G/dP$ reduced without significant changes in G bandwidth and 2D band intensity, as expected for a sample detachment process, unlike the results of Pimenta Martins *et al.*,[56] where $d\,\omega_G/dP$ increased with significant changes in G bandwidth and quenching of 2D band intensity. Therefore, Pimenta Martins *et al.* attributed the change in $d\,\omega_G/dP$, to changes in the mechanical properties of the system. For the evidence of transparency, the authors observed changes in the optical contrast images of the flakes in the same 4–7 GPa pressure range of the changes in the Raman spectra, culminating in the detection of a Raman peak from the SiO_2/Si substrate underneath the graphite flake after 7 GPa, indicated a gradual surface-to-bulk increase in transparency due to the phase transition process. Finally, for the evidence of hardness, the authors observed indentation marks on the SiO_2/Si substrate from a four-layer graphene and graphite samples compressed up to 8 GPa, from AFM topographic measurements as shown in Figs. 3(f)–3(j). The fact that SiO_2 is significantly harder than graphene systems (Vickers hardness of 564.9 kgf/mm^2 for amorphous SiO_2 compared to 7–11 kgf/mm^2 for graphite) is evidence that the indentation can only be explained by the formation of a hard phase upon compression. Furthermore, they reported the lowest critical pressure (approximately 4 GPa) and pressure-induced transparency (completed at approximately 7 GPa) in graphite, which was attributed to the role of water in facilitating the phase transition. Their theoretical models, based on molecular dynamics simulations and first-principles calculations, described a novel phase transition mechanism for compressed graphene systems in the presence of passivation groups on the surface layers. This model shows a gradual surface-to-bulk phase transition process, which starts with the sp^2–sp^3 rehybridization of the first two layers, forming diamondene and then propagates along the c axis to the bottom with increasing pressure.

D. Pressure-tuning of the electronic band structure in monolayer TMDs

The electronic band structure of monolayer semiconducting TMDs is highly sensitive to the effects of strain, therefore the application of hydrostatic pressures can induce profound changes in their band structure, and those changes can then be probed via Raman and photoluminescence spectroscopy. In the monolayer limit, these materials are direct-gap semiconductors forming two spin-valley locked and spin-split valleys at the K/K′ points in the BZ as shown in Fig. 4(a). Apart from the K/K′ valleys, semiconducting TMDs also posses six Q/Q′ valleys in the conduction band located roughly halfway between the Γ and the K points as shown in Fig. 4(a), which are also spin-valley locked and spin-split. However, phenomena involving K and Q scattering have been relatively unexplored. An important example of the potential of multivalley physics in TMDs is the observation of superconductivity in ion-gated few-layer semiconducting MoS_2.[94] The origin of this multivalley superconductivity was attributed to an increase in the electron–phonon coupling upon gating due to the appearance of new scattering channels, such as K–Q and Q–Q scattering, formed upon Fermi level crossing of K and Q valleys.[94] However, those multivalley effects are usually absent in monolayer TMDs due to the large energy difference between K and Q valleys ($\Delta\epsilon_{K-Q}$). Pressure has the effect of shifting the energies of the K/K′ and Q/Q′ valleys, causing a bandgap opening and a reduction in $\Delta\epsilon_{K-Q}$, possibly unlocking new multivalley physics phenomena.[59]

We will start the discussion with the bandgap opening effect induced by pressure. Nayak *et al.*[95] compressed monolayer semiconducting MoS_2 on SiO_2/Si up to 30 GPa using a neon PTM at ambient temperature and observed a blueshift of the PL from 1.85 eV at ambient pressure to 2.08 eV at 16 GPa—an increase in approximately 12% of the bang gap, assuming a constant exciton binding energy. Above 16 GPa the authors observed a quenching of the PL signal which they attributed to a crossover of the bandgap from direct to indirect due to a change of the valence band minima (VBM) from K to Γ, as indicated by their DFT calculations. Fu *et al.*[96] also reported a bang gap opening in compressed monolayer MoS_2 but the PL quenching was observed at a much lower pressure, around 5 GPa as shown in Fig. 4(b). The authors also attributed the quenching to a direct to indirect transition, however, due to a change of the conduction band minima (CBM) from K to Q at a pressure of 1.9 GPa. The crossing of the K and Q valleys was supported by DFT calculations and by monitoring the energy of the predominant peak in the PL, with pressure. A mixing of the energies of the K and Q valleys upon reduction of $\Delta\epsilon_{K-Q}$ would cause a deviation from the linear evolution of the predominant PL peak. A banggap opening and PL quenching was also observed in compressed WSe_2[97] [see Fig. 4(c)]. The authors also reported a K–Q crossing at approximately 2.2 GPa by monitoring the negatively charged exciton (trion X^-) peak of WSe_2 with increasing pressures and noticing its deviation from the linear behavior as seen in Fig. 4(d). Such deviation could be explained by the joint contributions to the PL signal from direct K–K and indirect K–Q transitions of the trions populating both K and Q valleys near K–Q crossing. Similar to the work of Fu *et al.*,[96] the pressure evolution of X^- could be fit by a model considering mixing of K and Q valleys with increasing pressure upon reduction of $\Delta\epsilon_{K-Q}$, as done for the Γ and X sate mixing upon Γ–X crossing in compressed quantum dots.[98]

Recently, it has been demonstrated that the modifications induced by pressure in the band structure of TMDs can be probed by monitoring the changes in the intensity and shape of the 2LA Raman band.[59] The 2LA band is present in the Raman spectra of all semiconducting TMDs, and it is composed of several modes arising from two-phonon double-resonance Raman process involving electronic scattering between K and Q as well as K and K′ valleys. The process is illustrated in Fig. 4(e). It starts with the absorption of a photon near the K valley and the creation of an electron–hole pair. Then, the excited electron is scattered either to K′ or to the Q valley by the creation of a phonon with momentum K for K–K′ scattering, or with momentum M for K–Q scattering. From momentum conservation, the electron is scattered back to the K valley by the creation of a second phonon with opposite momentum, then the electron–hole pair recombines and a photon is emitted. The Raman spectra of MoS_2 is shown in Fig. 4(f), where the 2LA modes arising from K–K′ (K–Q′) scattering are highlighted in red (blue). Pimenta Martins *et al.*[59] compressed monolayer MoS_2 and WS_2 on a SiO_2/Si substrate using 4:1 methanol:ethanol PTM and observed an enhancement of the 2LA band intensity for both materials as shown in Fig. 4(g) for MoS_2. They attributed the enhancement to the combined effects of a bandgap opening and a reduction of $\Delta\epsilon_{K-Q}$ at high pressures, which would increase the probability of K–K′ and K–Q scattering events. The bandgap opening blueshifts the B exciton energy (2.08 eV under ambient conditions and 2.13 eV at 4.5 GPa) closer to the laser excitation (2.33 eV), bringing the system closer to a resonant absorption/emission condition. The K–Q crossing would resonantly enhance the probability of K-Q scattering events since upon crossing, the scattering from K to Q would involve a real intermediate state instead of a virtual one as under ambient conditions, as represented by MoS_2 in Fig. 4(h). The K–Q crossing occurred near 3 and 2 GPa for MoS_2 and WSe_2, respectively, as evidenced by monitoring the evolution of their PL spectra. The authors pointed out that being able to probe multivalley scattering as a function of strain in monolayer TMDs should elucidate several phenomena including valley coherence and multivalley superconductivity.[59]

E. Pressure-tuning of the electronic structure in TMD heterostructures

Heterostructures of MX_2 TMDs typically form type II band alignment systems where the conduction band minina and the valence band maxima reside in opposite layers. Thus, upon photo excitation, a charge transfer process will occur where electrons and holes will accumulate on different layers as shown in Fig. 5(a). Due to the reduced dielectric screening and short interlayer distance, they will form bound electron–hole pairs where the carriers reside in opposite layers, these states are known as interlayer excitons (IXs). Their optical signature is a photoluminescence peak formed upon recombination of those electron–hole pairs, with the peak energy being smaller than the energies of the intralayer excitons from the individual layers. Pressure is a particularly important external tuning parameter to investigate those excitations since it reduces the interlayer distance directly modulating the IX energy. Xia *et al.*[100] compressed a 2H-stacked CVD grown $MoSe_2$/WSe_2 heterostructure and monitored changes in its electronic structure by analyzing the evolution with pressure of the IX photoluminescence peaks. The $MoSe_2$/WSe_2 heterostructure was directly transferred to the diamond's culet and they used silicone oil as the PTM. Figure 5(b) shows the evolution of the IX PL spectra. Below 1 GPa, it consisted in two peaks termed as I_A and I_B, which according to their DFT calculations would correspond to a direct IX electron–hole pair recombination at K and an indirect IX recombination from Y to K, as indicated in Fig. 5(c). Absorption measurements confirmed this scenario by the detection of an exciton peak with the same energy as I_A and the absence of a peak with the I_B energy. Above 1 GPa, the PL spectra

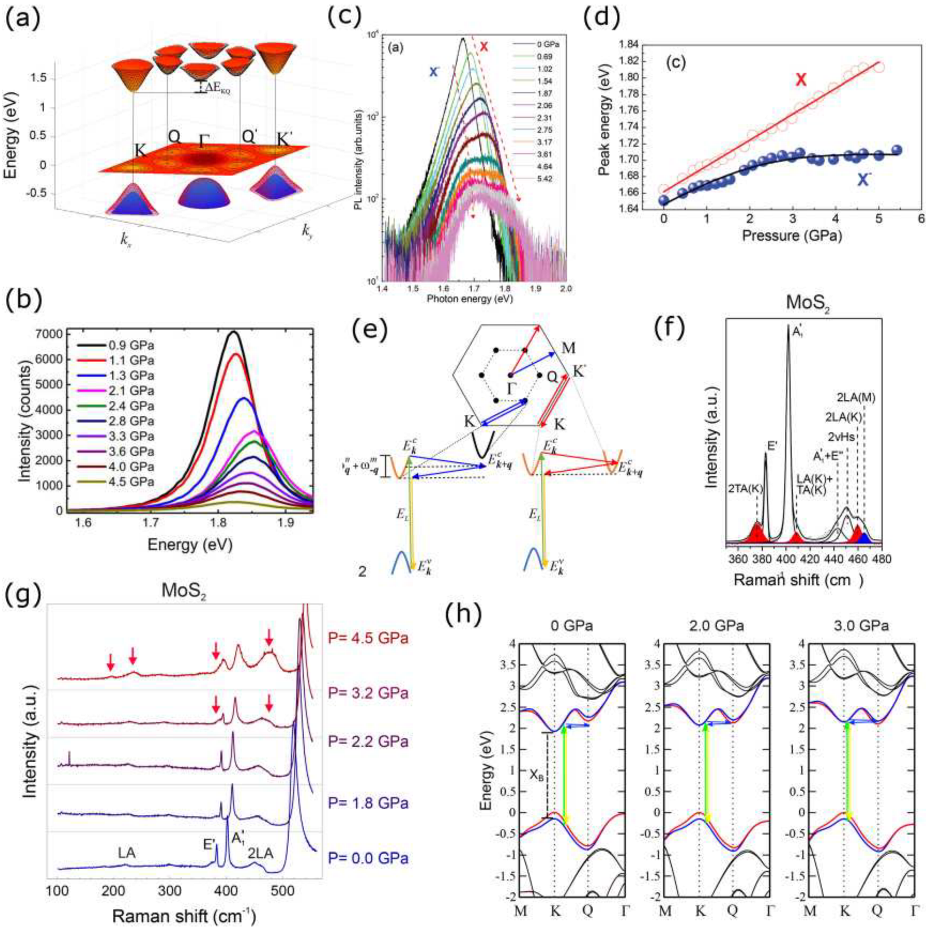

FIG. 4. Pressure-tuning of the electronic band structure in monolayer TMDs. (a) Electronic band structure of monolayer MX_2 TMDs under ambient conditions, where M is either Mo or W and X is either S or Se. The features shown here are common to all monolayer MX_2 TMDs. The two valleys at K/K′ and the six valleys at Q/Q′ are spin-split and exhibit spin-valley locking. The energy difference between K and Q valleys (ΔE_{K-Q}) ranges from tens to hundreds of meV depending on the TMD.[99] (b) Photoluminescence spectra of monolayer MoS_2 at increasing pressures. Reprinted with permission from Fu *et al.* Sci., Adv. **3**, e1700162 (2017). Copyright 2017 Authors, licensed under a Creative Commons Attribution 4.0 License. (c) Photoluminescence spectra of monolayer WSe_2 at increasing pressures with the dashed lines indicating the exciton (X) and trion (X^-) peaks. (d) Pressure evolution of the X and X^- energy for monolayer WSe_2. [(c) and (d)] Reproduced with permission from Ye *et al.*, Nanoscale **8**, 10843–10848 (2016). Copyright 2016 Royal Society of Chemistry. (e) Schematics of the two-phonon double resonance Raman processes that gives rise to the modes composing the 2LA band for MoS_2 and WSe_2. Upon absorption of a photon and creation of an electron–hole pair near K, the excited electron is scattered to K′ (Q) valley by the emission of a phonon with momentum K (M). The excited electron is then scattered back to K by the creation of a second phonon with opposite momentum and the electron–hole pair recombines emitting a photon. (f) Raman spectra of monolayer MoS_2 highlighting in red (blue), modes arising from two-phonon K–K′ (K–Q) scattering processes. (g) Raman spectra of monolayer MoS_2 with increasing pressures at 10 K. The red arrows indicate an enhancement of the intensity of the 2LA and LA bands. (h) DFT calculations for the band structure of monolayer MoS_2 with increasing pressures. Red and blue represent the different spin-polarized bands. The arrows represent the Raman processes associated with K–Q scattering at different pressures. Red and yellow arrows represent absorption and emission of a photon near the B exciton energy, while blue arrows represent spin-conserving phonon-assisted electronic scattering between K and Q valleys. [(a) and (e)–(h)] Reprinted with permission from Pimenta Martins *et al.*, ACS Nano **16**, 8064–8075 (2022). Copyright 2022 American Chemical Society.

changes drastically, giving rise to two features termed as I_C and I_D, which according to DFT calculations would correspond to an indirect IX electron–hole pair recombination from K and Y to Γ, respectively, as indicated in Fig. 5(d). Notice that the effect of pressure was to change the VBM from K to Γ, which could be directly probed by the changes in the PL features. Above 3 GPa, the authors observed a quenching of the PL signal, being consistent with the indirect nature of the I_C and I_D IXs PL peaks.

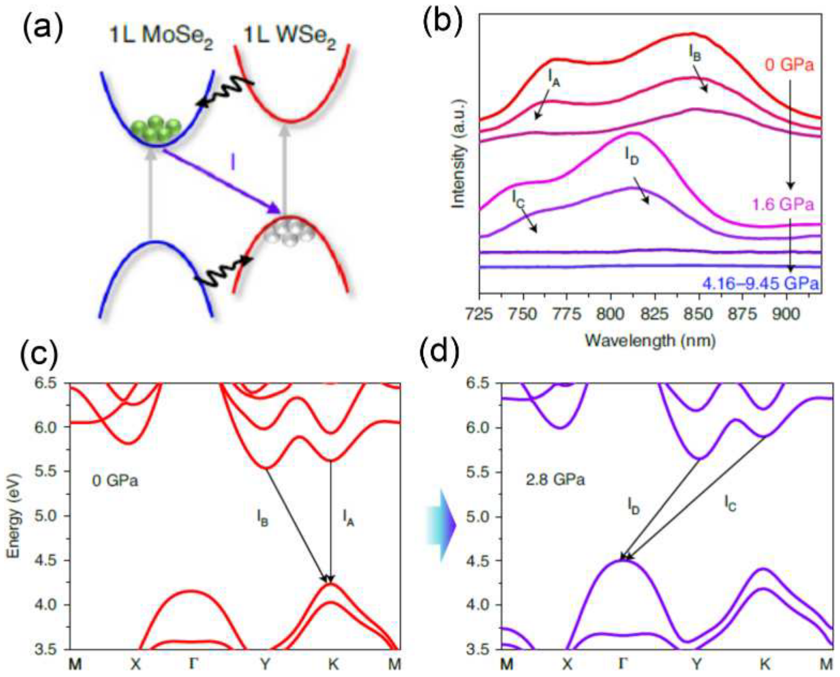

FIG. 5. (a) Schematics of a type-II band alignment between MoSe$_2$ and WSe$_2$, which is typical of MX$_2$ TMD heterostructures. Upon photoexcitation, electrons will accumulate in MoSe$_2$ and holes will accumulate in WSe$_2$, forming interlayer excitons (IXs). (b) Photoluminescence spectra of IXs of MoSe$_2$/WSe$_2$ with increasing pressures. (c) and (d) DFT calculations of the MoSe$_2$/WSe$_2$ band structure at ambient (c) and 2.8 GPa (d), where the origin of the PL peaks I_i ($i = $ A, B, C, and D) are indicated. Reprinted with permission from Xia *et al.*, Nat. Phys. **17**, 92–98 (2021). Copyright 2021 Springer Nature.

III. HIGH-PRESSURE EXPERIMENTS WITH PISTON-CYLINDER PRESSURE CELLS

A. Instrumentation and experimental technique

1. Piston-cylinder cell assembly and operation

The piston-cylinder pressure cell was invented in the late 1800s[101] and has since been employed across multiple fields of fundamental science including condensed matter physics and geology. Although many variations of the piston-cylinder cell geometry have been developed over the years, all involve positioning a sample within a bath of a PTM and systematically compressing the sample enclosure with a metal piston to raise the pressure. Most piston-cylinder cells can support the application of pressure $\lesssim$3 GPa, although somewhat higher pressure is possible with great care. Although this is orders of magnitude smaller than the maximum achievable pressures in diamond anvil pressure cells (discussed in detail in Sec. II), piston-cylinder cells afford orders-of-magnitude larger sample volume and are generally much easier to operate.

Figure 6(a) shows a schematic illustration of a piston-cylinder cell. The main body of the cell comprises a metal cylinder with a small-diameter hole bored axially through its center. Although the body of the cell can be machined from a single piece of ultra-hard metal, modern piston-cylinder cells achieve the highest pressures by utilizing a hybrid double-wall design in which an inner metallic cylinder is tightly fit within an outer metallic sleeve. Hard non-magnetic metals are generally desirable for condensed matter experiments; cells are typically constructed with a CuBe outer sleeve and a superalloy inner shell (e.g., NiCrAl).

The sample of interest is mounted atop a CuBe stage, which is initially detached from the main cell body. A Teflon cup filled with the desired PTM is positioned onto the sample stage, thereby sealing the sample completely within the PTM. The entire sample assembly fits tightly into the bore of the pressure cell body, such that the sample resides roughly in the geometric center of the cell. A metal piston, typically made from WC, sits atop the Teflon cup. Locking nuts enclose the assembly on each end of the cell. The pressure is controlled by applying force to the piston with a hydraulic press, thereby compressing the Teflon cup and reducing the volume of the sample space. The locking nut holding the piston in place is tightened as the Teflon cup is compressed, maintaining the pressure in cell even upon removing the load from the hydraulic press. After achieving the desired pressure at room temperature, the entire pressure cell can be affixed to an insert for cryogenic measurements. Piston-cylinder pressure cells can be operated down to millikelvin temperatures and in magnetic fields in excess of 40 T. However, changing the pressure requires warming the cell to room temperature and temporarily reloading it into the hydraulic press.

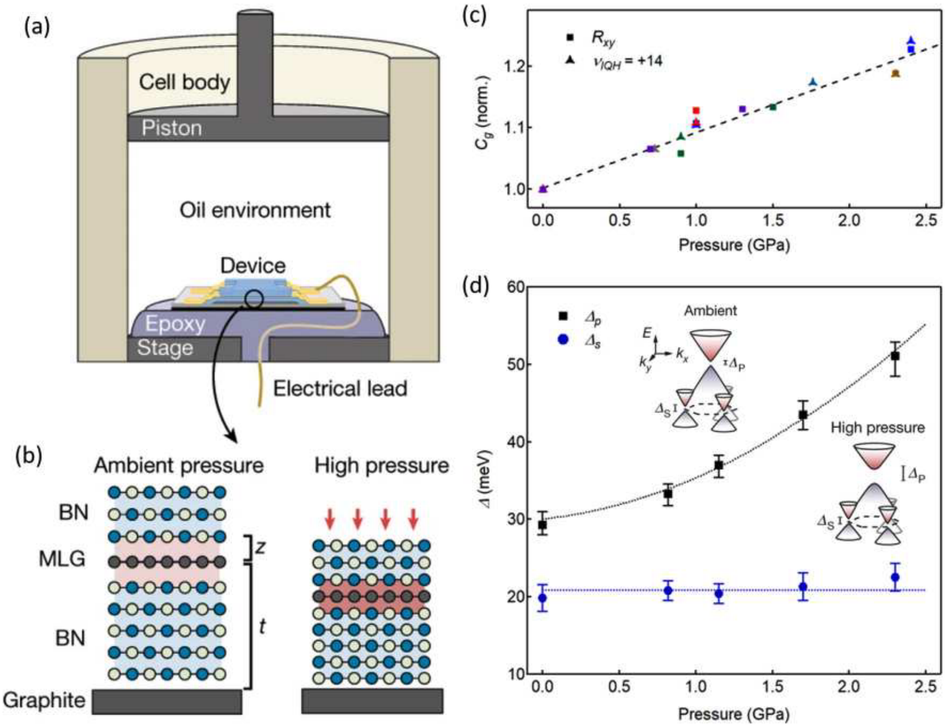

FIG. 6. (a) Schematic of a vdW heterostructure device residing inside a piston-cylinder pressure cell. (b) Schematic of a monolayer graphene sheet encapsulated between boron nitride crystals and resting on a flake of graphite. All of the layers compress toward each other under pressure. (c) Measurement of the gate capacitance, C_g, as a function of pressure in devices of graphene encapsulated by BN with a graphite back gate. Square (triangle) markers denote quantities extracted from measurements of the low-field Hall resistance (the integer quantum Hall gap with filling factor $\nu_{IQH} = +14$). Colors represent measurements from different devices. (d) Bandgap of the primary Dirac point (black squares) and the secondary Dirac point in the valence band (blue circles) as a function of pressure in an aligned graphene/BN device. The insets show cartoon illustrations of the graphene band structure at ambient and high pressure. Adapted with permission from Yankowitz *et al.*, Nature **557**, 404–408 (2018). Copyright 2018 Springer Nature.

2. Electrical characterization of vdW samples

In order to perform electrical transport measurements of samples under pressure, wires must penetrate into the sample space without allowing the PTM to leak out of the cell. To achieve this, a thin hole is drilled through the center of the sample stage prior to mounting the sample. A handful of insulated wires are threaded through this hole and epoxied into place (e.g., using Stycast), forming a leak-tight seal that can withstand at least one pressure campaign. The sample is then mounted atop the epoxy, and the wires are attached to the sample as desired. The pressure inside the sample space can be determined either optically or electrically. In the former case, an optical fiber is also inserted into the sample space through the stage, and ruby crystals are mounted near the end of the fiber. The fluorescence of the ruby crystal is used to measure the pressure. In the latter case, additional wires can be used to measure the resistance of pressure-sensitive metals in a four-terminal configuration. Typically, a coil of manganin wire is used to calibrate the pressure at room temperature, whereas the superconducting transition temperature of tin is measured for low-temperature calibration.

Creating electrical contacts to bulk materials is relatively straightforward, as the ends of the wires are simply pasted onto the sample. However, establishing electrical contact to vdW devices presents additional challenges since they typically reside on planar Si/SiO$_2$ wafers and are highly sensitive to electrostatic discharge. Various schemes have been employed recently to overcome these challenges, including carefully affixing the wafer to the epoxy and hand-pasting wires one-by-one onto the sample electrodes,[102] and using designer printed circuit boards compatible with wire bonding for sample mounting.[103]

3. Modifying the interlayer spacing between vdW crystals with pressure

The pressure inside the sample space of the piston-cylinder cell is very nearly hydrostatic, assuming a suitable choice of PTM. However, substrate-supported vdW heterostructures are highly anisotropic; the

Young's modulus of typical vdW crystals is orders of magnitude larger in the 2D plane than in the out-of-plane stacking direction,[104] and the sample rests on a Si/SiO$_2$ wafer on one side but is exposed directly to the PTM on the other. The latter complicates the relationship between the applied pressure and the lattice compression of the vdW crystals in the 2D plane. However, since the sample is much more deformable in along the vdW-stacked axis, the dominant effect of pressure is to reduce the interlayer spacing between all neighboring vdW crystals [see schematic in Fig. 6(b)].

Yankowitz *et al.*[102] established the relationship between pressure and interlayer spacing by investigating transport in heterostructures of graphene encapsulated by boron nitride (BN) crystals. A flake of graphite positioned beneath the bottom BN dielectric acts as a back gate electrode. The graphene charge carrier density, n, is directly related to the applied gate voltage, V_g, by the gate capacitance per unit area, C_g, following the relationship $C_g = en/V_g$, where e is the charge of the electron. Figure 6(c) shows measurements of C_g for a handful of such devices, normalized to its value at ambient pressure. For each data point, C_g is extracted by determining the value of n at a given V_g from the low-field Hall effect or by tracking the position of a certain integer quantum Hall state. The gate capacitance can be written equivalently as $C_g = \epsilon\epsilon_0/t$, where ϵ is dielectric constant of BN, ϵ_0 is the vacuum permittivity, and t is the thickness of the BN; thus, changes in both ϵ and t contribute to its evolution with pressure. Although these two quantities cannot be independently determined in the transport experiments, comparison to *ab initio* calculations reveal that the interlayer spacing of the BN decreases by approximately 2.5% per gigapascal of applied pressure. Roughly similar compression is also likely for other vdW materials, as well as for interfaces between dissimilar crystals, since all such layers are held together by a similar vdW adhesion.

B. Moiré materials under pressure

Heterostructures of vdW materials can be assembled by mechanically stacking various atomically thin crystals atop one another. A geometric interference effect known as a moiré pattern emerges when neighboring vdW crystals are rotationally faulted and/or lattice mismatched. The moiré pattern acts as a periodic potential for charge carriers in the heterostructure, and can have a wavelength many times larger than the atomic unit cells of the constituent crystals. Moiré patterns were imaged by scanning tunneling microscopy in graphene rotated on graphite[105] and graphene aligned with BN[106–108] over a decade ago, but the study of moiré materials expanded rapidly following the 2018 discoveries of superconductivity and strongly correlated states in magic-angle twisted bilayer graphene (tBLG).[12,109] Numerous techniques have been developed to control the moiré wavelength, including the "brute-force" method of simply fabricating many samples with different twist angles, aligning straight crystalline edges,[110] or by dynamically rotating one crystal atop another using an atomic force microscope tip.[111,112] Equally important is the amplitude of the moiré potential, which is dictated by the strength of the interlayer electronic coupling between the constituent vdW crystals. This coupling is set by the interlayer spacing between the crystals. Pressure therefore represents a distinct experimental tuning knob to modify the properties of moiré materials, as it directly controls the strength of the moiré potential by enhancing the interlayer electronic coupling.

1. Angle-aligned graphene/BN

The low-energy band structure of graphene is strongly modified when it is in close rotational alignment with BN. The moiré potential creates secondary Dirac points at finite energy in the graphene band structure,[108] opens a gap at the Dirac point by breaking the sublattice symmetry of the graphene,[113] and generates a recursive Hofstadter butterfly spectrum in a magnetic field.[110,113,114] These features depend both on the moiré wavelength and its amplitude. Under pressure, the energy gap of the Dirac point grows superlinearly owing to an enhancement of the moiré amplitude [Fig. 6(d)]. Surprisingly, the gap at the secondary Dirac point in the valence band appears to be roughly insensitive to pressure. The graphene lattice is known to strain on the moiré scale both in- and out-of-plane, and the details of this strain field also depend on pressure. Theoretical modeling suggests that the modifications of the graphene strain profile may reduce the gap at the secondary Dirac point in nearly equal magnitude to the amount it is enhanced by the larger moiré amplitude, resulting in an approximate compensation.[102]

2. Twisted bilayer graphene

The low energy bands of tBLG become extremely flat when the two graphene sheets are twisted very near the "magic angle" of 1.1°. Coulomb interactions between electrons become dominant in such samples, leading to the emergence of superconductivity and a variety of strongly correlated and topological states.[115,116] The ratio of Coulomb to kinetic energy (U/K) grows continuously as the twist angle is tuned away from the magic angle, in principle enabling a careful mapping of the correlated phase diagram as the strength of the many-body interactions is varied. Although impressive progress has been made in this direction, a full understanding has been complicated by random inhomogeneous strains that form during sample fabrication, uncontrolled and unknown alignment of the encapsulating BN crystals, and the requirement of fabricating and studying many samples with slightly different twist angles.

Pressure provides an alternative pathway toward tuning U/K within a single tBLG device, stemming from the similar roles of twist angle and interlayer coupling strength in determining the band structure. A "magic angle" is possible for a wide range of angles just above 1°, simply requiring the application of pressure to enhance the interlayer coupling and flatten the band. Figure 7(a) shows transport measurements of a tBLG device with a twist angle of 1.27° both at 0 GPa and at 2.21 GPa. Correlated states at integer band filling factors (ν, where $\nu = \pm 4$ corresponds to full filling of the flat bands, and is alternatively referred to as $\pm n_s$) are nearly absent at 0 GPa, and no signatures of superconductivity are observed down to a base temperature of 300 mK. In contrast, at 2.21 GPa correlated insulating states are clearly seen at $\nu = -2, +1, +2$ and $+3$, and superconductivity is observed for a region of hole doping just beyond $\nu = -2$ [Fig. 7(b)]. Additional measurements at 1.33 GPa show that the energy gaps of the correlated insulators and the critical temperature of superconductivity evolve non-monotonically with pressure [Figs. 7(c)–7(d)]. The non-monotonic evolution of the apparent strength of correlations follows the theoretical expectation that the band should be maximally flat at a pressure of approximately 1.5 GPa for a sample at this twist angle.[117,118] Future experiments mapping out a higher density of

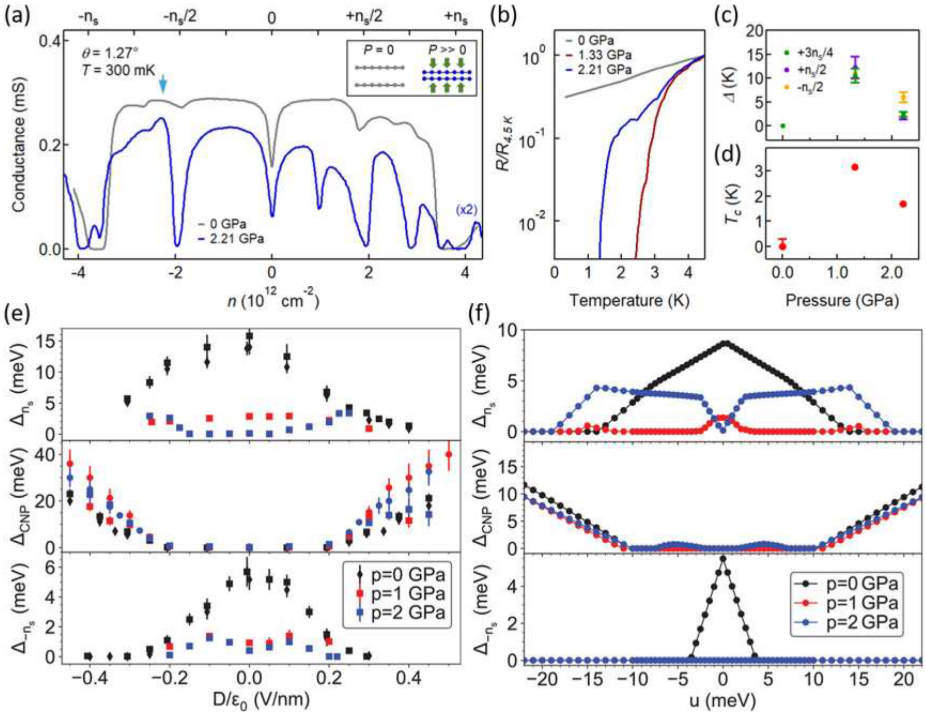

FIG. 7. (a) Conductance of a tBLG device with a twist angle of 1.27° measured at 0 (gray) and 2.21 GPa (blue), acquired at a temperature of 300 mK. (b) Temperature-dependence measurements of the device resistance at various pressures acquired at doping indicated by the blue arrow in (a). The sample is metallic at 0 GPa and superconducting at higher pressure. (c) Thermally activated energy gaps of the correlated insulating states at half and three-quarters filling of the flatband as a function of pressure. (d) Pressure-dependence of the superconducting critical temperature, T_c. [(a)–(d)] Reprinted with permission from Yankowitz *et al.*, Science **363**, 1059 (2019). Copyright 2019 AAAS. (e) Measurements of the energy gaps in a tDBG device with a twist angle of 1.07° measured as a function of displacement field and pressure. (f) Theoretical estimates of the gaps calculated from the single-particle band structure. [(e) and (f)] Reproduced with permission from Szentpéteri *et al.*, Nano Lett. **21**, 8777 (2021). Copyright 2021 Authors, licensed under a Creative Commons Attribution License.

pressure points and in samples with different twist angles will help to further elucidate this physics.

3. Twisted double bilayer graphene

Many moiré materials beyond tBLG can develop flat bands driven by the superlattice potential, and in principle the correlated and topological properties of all such systems should also depend on pressure. Twisted double bilayer graphene (tDBG)—constructed by stacking and rotating two sheets of Bernal-stacked bilayer graphene[119–123]—has also been investigated under pressure.[124] At ambient pressure, tDBG exhibits relatively flat moiré bands over a wider range of twist angles than tBLG owing to additional band tunability in a perpendicular displacement field. Correlated insulating states and associated isospin symmetry breaking have been observed in devices with twist angles just above 1°. These correlated states exist roughly within a window of displacement field in which band gaps are open at both the charge neutrality point ($\nu = 0$) and full band filling ($\nu = \pm 4$). These gaps are anticipated by calculations of the single-particle band structure of tDBG and can be opened and closed depending on both the displacement field and pressure. Szentpéteri *et al.*[124] measured the pressure dependence of these gaps in a tDBG sample with a twist angle of 1.07° [Fig. 7(e)] and found that, in general, they were either weakly tuned ($\nu = 0$) or substantially decreased ($\nu = \pm 4$) as the pressure is raised. The evolution of these gaps with pressure is reasonably well explained by the single-particle band structure calculated with an enhancement in the interlayer coupling, shown in Fig. 7(f). Symmetry-broken states are only very weakly developed at this twist angle, so additional work remains necessary to map out the full evolution of the correlated and topological states in tDBG tuned by the combination of twist angle, doping, displacement field, and pressure.

C. Controlling 2D magnetism with pressure

A rapidly growing family of vdW magnets have been identified following the discovery of 2D magnetism in 2017.[125,126] Chromium triiodide (CrI_3) is a prototypical example of a 2D Ising ferromagnetic insulator, exhibiting out-of-plane ferromagnetism within each monolayer and antiferromagnetic interlayer coupling.[126] The layer-dependent magnetism of few-layer CrI_3 crystals has been probed in a number of distinct ways, including optically using reflective magnetic circular dichroism (RMCD)[126] and electrically in magnetic tunnel junction geometries.[127,128] Following the isolation of monolayer CrI_3, it was quickly recognized that the interlayer stacking configuration of the CrI_3 is likely connected to its interlayer magnetic ordering. The bulk CrI_3 crystal is known to undergo a structural transition from a monoclinic to rhomobohedral stacking configuration upon reducing the temperature below 220 K,[129] whereas Raman spectroscopy and second-harmonic generation measurements indicate that few-layer CrI_3 remains stacked in the monolinic configuration down to cryogenic temperatures[130] [see schematics in Fig. 8(a)]. Bulk crystals further exhibit interlayer ferromagnet ordering below the Curie temperature, in contrast to the interlayer antiferromagnetism found in few-layer CrI_3.

Song *et al.*[131] and Li *et al.*[132] simultaneously reported that pressure could be used to directly manipulate the magnetic ordering of few-layer CrI_3 by irreversibly altering its interlayer stacking configuration from monoclinic to rhombohedral. Figure 8(b) shows bulk tunneling measurements across a bilayer CrI_3 surrounded by graphite electrodes at a few different pressures, taken from Ref. 131. Hysteresis in the tunneling current, indicating the magnetic field at which the bilayer switches from interlayer antiferromagnetic to ferromagnetic, is found to persist to a pressure of at least 1.46 GPa. However, the hysteresis vanishes in the measurement performed at 2.70 GPa, indicating that the CrI_3 bilayer is a layer ferromagnet at all magnetic fields. The pressure-dependence of the interlayer magnetic ordering is further

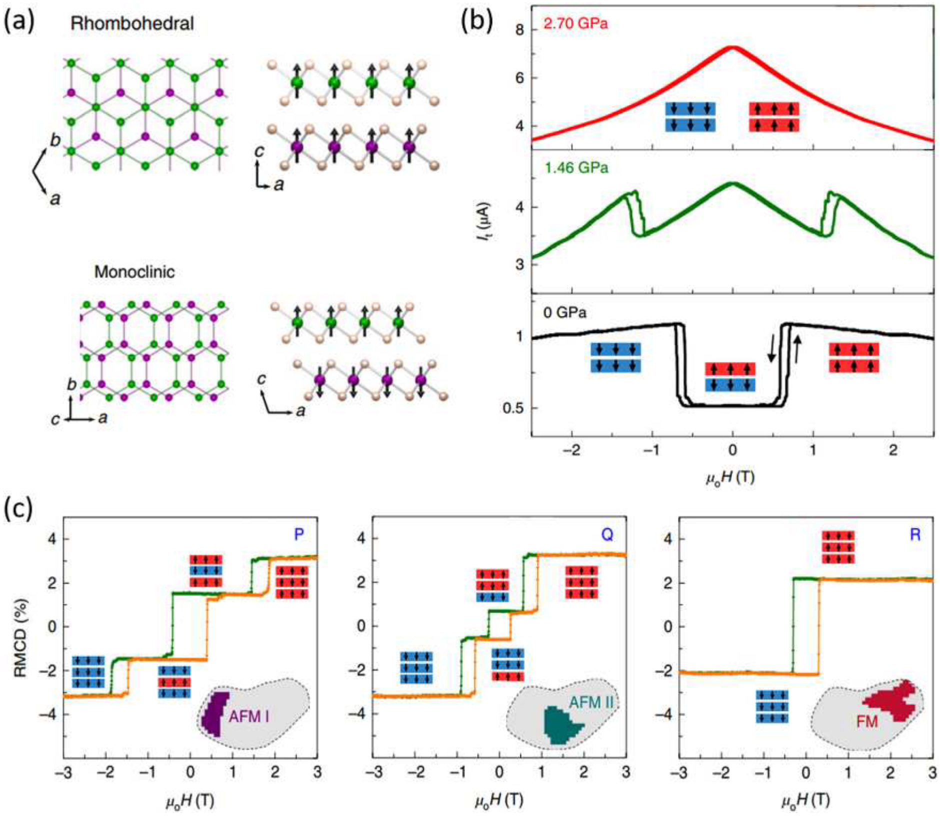

FIG. 8. (a) Schematic of the rhombohedral (top) and monoclinic (bottom) stacking configurations of bilayer CrI_3. The green (purple) atoms represent the Cr atoms in the top (bottom) layer, while the brown ones represent the I atoms. The top (side) view is shown on the left (right). The black arrows represent the magnetic ordering. (b) Tunneling current, I_t, vs magnetic field in a bilayer CrI_3 tunnel junction device acquired at a series of pressures. (c) RMCD measured at three different points on a trilayer CrI_3 flake, as indicated by the inset illustrations in the bottom right of each panel. The measurements are performed at 0 GPa after a pressure of 2.45 GPa was applied to the sample. The cartoon insets in (b) and (c) depict the magnetic states at each applied magnetic field. Adapted with permission from Song *et al.*, Nat. Mater. **18**, 1298–1302 (2019). Copyright 2019 Springer Nature.

confirmed by optical spectroscopy performed on the samples before and after the pressure cycle.

Figure 8(c) show RMCD measurements of a trilayer CrI$_3$ sample,[131] acquired after applying a pressure of 2.45 GPa to the sample and then unloading the pressure back to ambient. Three different types of magnetic ordering are observed, corresponding to different regions of the sample. Region R exhibits a single hysteresis loop surrounding $B = 0$, indicative of interlayer ferromagnetism. Regions P and Q are more complicated, with numerous step-like jumps in the RMCD and hysteresis surrounding numerous values of B. These regions correspond to two different forms of interlayer antiferromagnetism, as indicated by the schematic insets surrounding the data. The results indicate that sufficiently high pressure drives an irreversible monoclinic-to-rhombohedral conversion of the stacking order of the CrI$_3$, which persists even upon removing the pressure. Measurements of the polarization angle dependence of the Raman spectroscopy further corroborate this conclusion,[131,132] showing a fourfold polarization dependence indicative of monoclinic stacking prior to applying pressure, and an absence of polarization dependence indicative of rhombohedral stacking subsequent to applying pressure.

D. Pressure-tunable proximity effects

When dissimilar vdW crystals are stacked atop one another, proximity effects between them can modify the properties of each of the constituent crystals.[133] A well-studied example is the case of graphene on transition metal dichalcogenide (TMD) substrates. Although freestanding graphene has extraordinarily weak spin–orbit coupling (SOC) on the order of tens of μeV, the proximity effect from the TMD substrate can enhance it to values of a few meV.[134–139] Theoretical modeling, unsurprisingly, predicts that the value of the proximity-induced SOC grows rapidly as the interlayer spacing between the graphene and TMD is reduced.[135] Fülöp *et al.*[140] study the SOC in a graphene/WSe$_2$ heterostructure up to a pressure of 1.8 GPa. They extract the strength of the Rashba SOC from measurements weak antilocalization and estimate that it is enhanced by approximately a factor of two over the accessible range of pressure. These measurements highlight the great promise of using pressure to directly control proximity effects in vdW heterostructures.

IV. HIGH PRESSURE EXPERIMENTS USING SCANNING PROBE MICROSCOPY

In addition to diamond anvil cells and piston-cylinder cells, scanning probe microscopy (SPM) constitutes a family of techniques that enables the application of large axial pressures onto thin vdW materials. Using a hard tip at the end of cantilever, it is possible to apply pressure in the range of several GPa under a chosen and controlled environment (ambient, vacuum, or different atmospheres and temperatures). Through this approach, a variety of experiments have demonstrated the transformation of the parent vdW materials into novel phases with exquisite properties. In the following sections, we will describe some aspects of the required instrumentation (Sec. IV A), some representative studies of SPM-induced modification of several vdW materials (Sec. IV B) and a few other SPM-enabled tweaking of their electromechanical properties (Sec. IV C).

A. Instrumentation and experimental technique

Figure 9 schematizes the process of pressure application onto vdW materials via SPM. A sample, consisting of mono- to few-layered flakes of the chosen vdW material is placed (or grown) atop a hard and smooth substrate (a piece of doped Si wafer with a 300 nm-thick layer of Si oxide is a common choice) and, then, transferred onto any conventional SPM apparatus. The cantilever-tip system, an integral part of any SPM setup, provides the application of force (or pressure) onto the sample when it is brought into physical contact with the sample surface by piezoelectric actuators. The cantilever acts as a spring with a characteristic constant k, enabling the application of controlled forces upon its deformation against the sample surface. Through the variation of the cantilever material, geometry, dimensions and deformation, the applied force may range from picoNewtons to microNewtons. A tip, at the end of the cantilever, transfers the cantilever deformation force onto the sample, creating an effective sample deformation area S. Due to the nanometric dimensions of the tip end and the range of the applied forces, such tip-sample interaction area may range from few nm^2 up to hundreds of nm^2. Therefore, the effective applied pressure may range from few kPa up to tens of GPa. It is important to stress here that, different from DACs, where the applied pressure is isotropic, the SPM applied pressure has an axial nature and its value may vary across the effective deformation area S (being larger at the center and smaller at the border). Moreover, it is a localized effect. In other words, only the region of the sample directly beneath the SPM tip is eventually modified, with the remaining vdW material remaining unchanged.

As a consequence of its working mechanism and considering the relation between applied force and applied pressure in typical SPM experiments, the exact estimation of pressure values is not trivial. It requires the use of an approximate contact mechanics model (there are several: Hertz, JKR, DMT, Maugis, and others), the precise value of the tip radius R and the precise value of the sample deformation d under the applied force to estimate S (and, therefore, P).[141,142] For example, using the simplest model—Hertz model for non-adhesive elastic deformations—the radius a of the contact area can be estimated as $a = (R.d)^{1/2}$, where R is the tip radius and d is the deformation of the vdW material.[141,142] In most cases, the value of R is typically within the range between 10 and 30 nm and d is in the range of 0.1–1 nm.

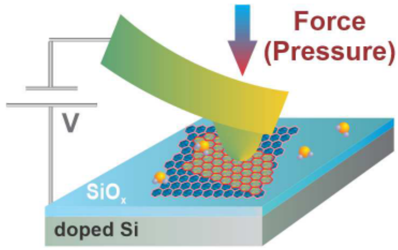

FIG. 9. Schematic illustration of SPM-controlled modification of vdW materials via pressure application. The tip at the end of a cantilever (in yellow-green shades) compresses the vdW layers (blue-green shades) placed (or grown) atop a hard substrate (e.g., doped Si covered with a thin Si oxide layer). In addition to the mechanical characterization, the SPM apparatus also enables electrical characterization via application of a bias V between tip and sample.

This gives a contact radius a in the range between 1 and 6 nm. Using P = F/S, where P (F) is the applied pressure (force) and S is the area of contact S = πa^2, one gets a typical pressure of 10 GPa for an applied force around 300 nN and a contact radius of around 3 nm. Theoretically and within the Hertz model, the deformation d increases with applied force F as d = $\{9F^2/[16(RE')^2]\}^{1/3}$, where E′ is the reduced elastic modulus given by $1/E' = (1-\nu_1^2)/E_1 + (1-\nu_2^2)/E_2$ and E_1 (E_2) are the elastic moduli and ν_1 (ν_2) are the Poisson's ratios associated with SPM tip and vdW flake, respectively.[142] Hence, the radius a of the contact area grows with applied force F as $a = (3RF/4E')^{1/3}$.[141,142] Even though this equation shows a simple relation between applied force and contact area, it depends on the reduced elastic modulus E′, which has a complicated convolution between the elastic properties of the ultrathin vdW flake and its supporting substrate. In other words, the experimental determination of E′ is non-trivial and, thus, the experimental determination of the contact area is non-trivial (and prone to significant approximation errors). Therefore, due to these large uncertainties in the quantitative values of the contact area, most SPM pressure-related studies prefer to use experimental force values, which are much more precise and much less model-dependent than experimental pressure values. Nevertheless, there are sub-nanometer indentation techniques, where the substrate effect is well modeled and, thus, the tip pressure determination is more reliable.[143]

The role of SPM in pressure-modification of vdW materials goes beyond the modification itself and includes some characterization possibilities as well. Since the pressure-induced modifications of vdW materials involve mechanical and/or electrical changes in the parent material, different SPM techniques, such as force spectroscopy, conductive AFM, electrostatic force microscopy (EFM), and scanning Kelvin force microscopy (SKPM), can also be used to probe such electromechanical effects. In force spectroscopy, the same procedure used to apply pressure onto the vdW material is used to record force-displacement curves, which can be analyzed based on some contact mechanics models and yield information about hardness and/or elastic modulus of the modified material.[141,142] Regarding electrical characterization, a common technique is conductive AFM (c-AFM), where a bias is applied between the AFM tip and sample and the flowing electrical current is monitored. Albeit being an efficient characterization method, c-AFM requires either a conducting substrate where the vdW is placed on or a direct electrical contact to the flake (which requires sophisticated lithography processes). Nevertheless, there are two other electrical SPM techniques that do not require direct electric contact with the vdW flake: EFM and SKPM, which characterize free charges, dielectric properties and work function variations.[141,144] A common approach involves the use of a biased AFM tip to transfer electric charges to the vdW material, while applying the desired pressure, and the efficiency of this process is analyzed via EFM imaging.[145–147] Specifically, in the charging process, a biased AFM tip is kept in contact with a given region (a single point—without any scanning) of the vdW material during a constant contact time (typically, t = 0.1 s[145–147]) transferring charges to it. After injection, the extra charges on the sample induce image charges of opposite sign in the EFM tip during the scan, where the tip is kept at a distance z from the surface, leading to an attractive tip-sample interaction which shifts the cantilever oscillation frequency to lower values.[145–147]

Therefore, this EFM response $\Delta\omega$ can be directly correlated with the amount of injected charges q as follows: the general theory of EFM shows that the frequency shift $\Delta\omega$ measured in EFM images is proportional to the gradient of the electrostatic tip-sample force dF/dz due to the electric field E by

$$\Delta\omega = \frac{\omega_0}{2k}\frac{\partial F}{\partial z}, \qquad (4)$$

where ω_0 and k are the cantilever resonant frequency and spring constant, respectively.[141] The surface charge density σ ($\sigma = q/A$) in a given flake can be estimated from EFM images considering the electric field E of a disk of effective radius R. It is known that the electric field E at a distance z from the disk is

$$E = \frac{\sigma}{2\epsilon}\frac{1-z}{\sqrt{z^2+R^2}}, \qquad (5)$$

where ϵ is the electrical permittivity of the air. After some manipulation of Eqs. (4) and (5), it results that the charge density σ can be estimated by

$$\sigma = \sqrt{\frac{4k\epsilon\Delta\omega(z^2+R^2)^{3/2}}{\pi r^2 R^2 \omega_0}}, \qquad (6)$$

where r is the EFM tip radius. In other words, Eq. (6) states that the amount of charges q is directly proportional to the square-root of the EFM response: $q = \beta(\Delta\omega)^{1/2}$, where β is a constant. One should note that the above methodology does enable the estimation of the injected charge density σ in units of charge per area. However, as Eq. (6) shows, in order to calculate σ, one needs to know the value of R, which is the radius of the effective disk of charges interacting significantly with the EFM probe. Such an estimation of R should take into account the tip-flake distance, tip radius r and even dielectric/screening properties of the flake material. Thus, the estimation of R may become quite arbitrary and introduce an unnecessary source of quantitative error in the measured charge values. Therefore, in many cases, the value of β is left non-estimated and the results are expressed in terms of the EFM signal $\Delta\omega$, which are surely proportional to the real quantitative charge values.

Another important experimental issue for the correct investigation of the charging process is the relative humidity of the environment around a charged sample. Since the EFM methodology described above is relatively slow (it takes several minutes to acquire an EFM image), one needs to avoid any spontaneous discharging processes at this timescale if the correct values of q are to be estimated. Some works reported that water vapor molecules under ambient RH conditions are the main source for spontaneous discharge of electrified surfaces.[72,146] Therefore, for the correct estimation of the injected charge q, a dry environment (usually dry N_2 atmosphere) surrounding the sample is employed. SKPM characterization requires the application of both AC and DC biases between tip and sample (without any mechanical stimulation applied to the cantilever).[141] The presence of free charges on the sample and/or work function differences induce an oscillatory force between tip and sample at the same frequency of the applied AC bias.[141] Using appropriate DC bias applied to the tip and a feedback mechanism, it is possible to determine the sample's surface potential and eventual work function differences.[141,146]

B. Pressure-induced phase transition in 2D materials

As described above, SPM techniques enable simultaneous pressure-related modification and subsequent characterization of materials. This is exemplified in earlier studies with carbon nanotubes, where deformation-induced electronic transition is shown to occur in semiconducting nanotubes[145] or where the universal behavior of carbon nanotube deformation is demonstrated.[148] The first study of SPM-controlled pressure-induced phase transition in 2D materials was published in 2011,[72] where the room-temperature diamondization of few-layer graphene was evidenced via electrical measurements [see Figs. 10(a) and 10(b)]. Panel (a) shows the charging efficiency, which is proportional to the EFM frequency shift $\Delta\omega$, as a function of applied force (by the SPM tip) for monolayer and bilayer graphene. While the charging efficiency is constant for monolayer graphene (black symbols), it decreases significantly for bilayer (green symbols) and few-layer (not shown in this panel) graphene, which is a signature of gap opening and, thus, electrical evidence of the diamondization transition.[72,145] Structural evidence for such process [illustrated in the cartoon in Fig. 10(b)] were shown in a subsequent work using Raman spectroscopy at high pressures [see Fig. 3(a)].[9] The same process was also observed for bilayer graphene grown on SiC using force

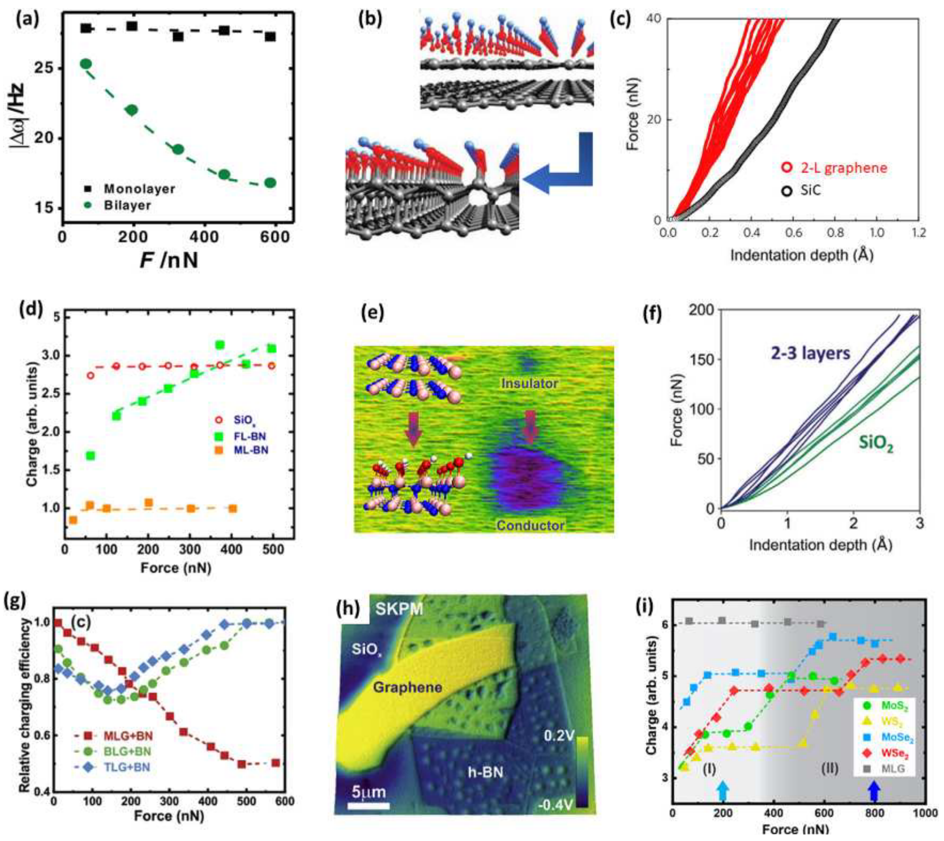

FIG. 10. SPM-controlled pressure-induced modification of vdW materials. (a) and (b) illustrate the process of graphene diamondization via pressure application [see the cartoon in (b)]. The graph in (a) shows a significant decrease in the charge transfer efficiency (measured as the EFM frequency shift $\Delta\omega$) as the applied tip force increases for bilayer graphene, indicative of gap opening. [(a) and (b)] Reproduced with permission from Barboza *et al.*, Adv. Mater. **23**, 3014–3017 (2011). Copyright 2011 John Wiley and Sons. A similar diamondization process is evidenced in mechanical measurements shown in (c), where bilayer graphene becomes harder as it is compressed by the SPM tip. (c) Reproduced from Gao *et al.*, Nat. Nanotechnol. **13**, 133 (2018). Copyright 2018 Springer Nature. (d) and (f) illustrate the pressure-induced modification of h-BN, either via electrical characterization [(d) and (e)] or mechanical characterization (f). The "diamondization" of h-BN leads to gap closure [(d) and (e))] and material hardening (f). [(d) and (e)] Reprinted with permission from Barboza *et al.*, ACS Nano **12** 5866 (2018). Copyright 2018 American Chemical Society. (f) Reproduced with permission from Cellini *et al.*, Adv. Sci. **8** 2002541 (2021). Copyright 2021 Authors, licensed under a Creative Commons Attribution License. The pressure effect on graphene/h-BN heterostructures is shown in panels (g) and (h), which show different electrical behaviors depending on the number of graphene layers atop a h-BN flake. The SKPM image in (h) readily differentiates graphene and h-BN layers and the substrate. [(g) and(h)] Reprinted with permission from Barboza *et al.*, Carbon **155**, 108–113 (2021). Copyright 2021 Elsevier. (i) Pressure-induced transitions in TMDs were also investigated via electrical SPM characterization, showing two distinct mechanisms of gap closure. Reproduced with permission from Bessa *et al.*, ACS Appl. Nano Mater. **4**, 11305 (2021). Copyright 2021 American Chemical Society.

spectroscopy [panel (c)] and conductive AFM.[73] The graph in Fig. 10(c) indicates significantly smaller indentation depths for bilayer graphene in comparison to the SiC substrate for the same applied tip force, evidencing a hardening effect of bilayer graphene upon pressure application.[73] This hardening effect was further confirmed via hydrostatic high-pressure experiments, where bi-, four-, and five-layer graphene samples were compressed in a water medium. After the onset of the phase transition, revealed by Raman spectroscopy and optical images, the SiO_2/Si substrate showed indentation marks along the edge of the samples[56] (see discussion in Sec. II C). Additional conductive AFM data under high pressure (data not shown) also show a decrease in electrical conductivity, consistent with the gap opening hypothesis.[73]

After the initial SPM studies with graphene systems, an immediate question arose regarding whether the same effect could be observed in other systems. The most natural candidate would be hexagonal boron nitride (h-BN), also dubbed as "white graphene," which has strikingly similar structure to graphene. However, opposite to graphene, h-BN is a wide bandgap material (6 eV) which may be used as a deep UV source.[149] Due to its structural similarities with graphene, monolayers and up to few-layers h-BN were investigated using the same SPM methodology initially applied to graphene as shown in Figs. 10(d) and 10(e). The graph in Fig. 10(d) shows that the charging efficiency of h-BN few-layers actually increase upon force (pressure) application by the SPM tip (green symbols), while the charging efficiency remains constant for monolayer h-BN and the Si oxide substrate (orange and red symbols, respectively).[146] Such increase in charging efficiency is indicative of gap closure,[145] suggesting that a 3D-rehybridized BN material would be a conducting material. This was indeed confirmed in an ensuing SPM experiment [summarized in panel, Fig. 10(e)]. The left side of Fig. 10(e) shows two structural models for bilayer h-BN: uncompressed 2D h-BN (upper model) and the proposed 3D-rehybridized h-BN structure (lower model).[146] The background image in Fig. 10(e) is an EFM image of a large h-BN few-layer flake [green-yellow shades in Fig. 10(e)]. A small square region ($\sim$2 μm^2)—on the low-right part of Fig. 10(e)—was continuously compressed (F = 300 nN), creating a rehybridized region.[145] Then, single point charging procedures were carried out on a pristine region of the h-BN flake [upper violet circle in Fig. 10(e)] and on the center of the rehybridized square region. Subsequent EFM imaging allowed the analysis of the charge spread in both pristine and modified regions. Being an insulator, electrical charges do not spread across the pristine h-BN and a small circular region is observed [upper violet circle in Fig. 10(e)]. However, the EFM image shows that the injected charge is homogeneously spread across the entire modified square region, evidencing the conducting nature of this new pressure-modified h-BN compound.[146] Another recent study indicates a similar 3D-rehybridization of h-BN using SPM-based compression, as illustrated in Fig. 10(f)[150]. Similar to the graphene case in panel (c), the graph in panel f indicates a noticeable hardening of 2–3 layer h-BN upon compression when compared to the Si oxide substrate, suggesting a similar "diamondization" effect of h-BN.[74,150]

Following the 3D-rehybridization processes shown to occur in graphene and h-BN,[72,73,76,146,150] it is only natural to wonder what would happen to a graphene/h-BN heterostructure under compression. Such question was answered in a SPM-based study where monolayer, bilayer and tri-layer graphene were placed atop h-BN flakes and the formed heterostructures were compressed and their electrical response analyzed.[147] Figures 10(g) and 10(h) illustrate the richness of phenomena occurring in such heterostructures under compression. The SKPM image in Fig. 10(h) shows the surface potential difference between a multilayered h-BN flake (in blue-green shades) and a tri-layer graphene flake (in yellow) placed atop it. Figure 10(g) summarizes the results for all investigated heterostructures in a graph of charging efficiency as a function of applied tip force. For the case of a monolayer graphene atop h-BN (red symbols), a significant decrease in the charging efficiency indicates gap opening with covalent bonding between graphene and h-BN layers (a process similar to the diamondization of graphene).[72,73,76,147] The phenomenology changes for the cases of bilayer (green symbols) and tri-layer (blue symbols) graphene atop h-BN. After an initial decrease in charge efficiency (indicative of gap opening) at small applied forces (pressure), both systems evolve to a final conducting state (increase in charging efficiency), similar to the case of h-BN under pressure,[146] as the applied force (pressure) increases.[147] Transition metal dichalcogenides (TMDs) constitute another important class of vdW materials with attractive optoelectronic properties.[1,151,152] Most TMDs are semiconducting materials with energy gaps in the 0.5–2 eV range[1,151,152] and some theoretical studies have proposed a pressure-induced gap closure for these materials,[153–155] which were indeed observed using different experimental techniques.[156–158] A recent SPM-based study has investigated four different TMDs and has shown two distinct pressure-induced gap closure process for each of them [see Figs. 10(i)].[159] The graph of charging efficiency as a function of applied tip force shows an initial increase in charge efficiency at low forces (pressure) for all TMDs (MoS_2, WS_2, $MoSe_2$, and WSe_2), which is associated with surface functionalization.[159] After well-marked plateaus, the charge efficiency increases again at higher applied forces (pressure), which is associated with structural changes in the TMDs (interlayer approximation and intralayer deformation).[153–159]

C. Pressure-tuning of properties of 2D materials

The use of SPM techniques to modify vdW materials via pressure application goes beyond the structural "diamondization" processes, including covalent bond formation, described above. There are also a few other examples of SPM-controlled pressure-modification of materials that lead to some interesting phenomena, as illustrated in Fig. 11. One such case uses a combination of pressure application and lateral tip movement to create a giant negative dynamic compressibility of some vdW materials (graphene, h-BN, MoS_2, and talc)[160,161]—see Figs. 11(a)–11(d). The contact mode AFM images in panels (a)–(c) show the apparent height (thickness) evolution of a bilayer graphene flake with the applied tip force (pressure) during the imaging scan: as the force (compression) increases, the bilayer graphene becomes apparently thicker. These seemingly counterintuitive results are summarized in the graph in panel (d), which shows the measured height profile of the flake for each applied force.[160] Such giant negative compressibility effect is actually the result of a pressure-dependent shear effect which induces flake corrugations as the tip is scanned across its surface.[160] The effect of tip-induced deformation was also observed for epitaxial graphene grown on SiC[162,163] and graphene on h-BN.[164] As illustrated in Fig. 11(e), there is a measurable deformation of the epitaxial graphene as the AFM tip-sample interaction increases.[162] A similar study explores the possibility of pressure-induced commensurate

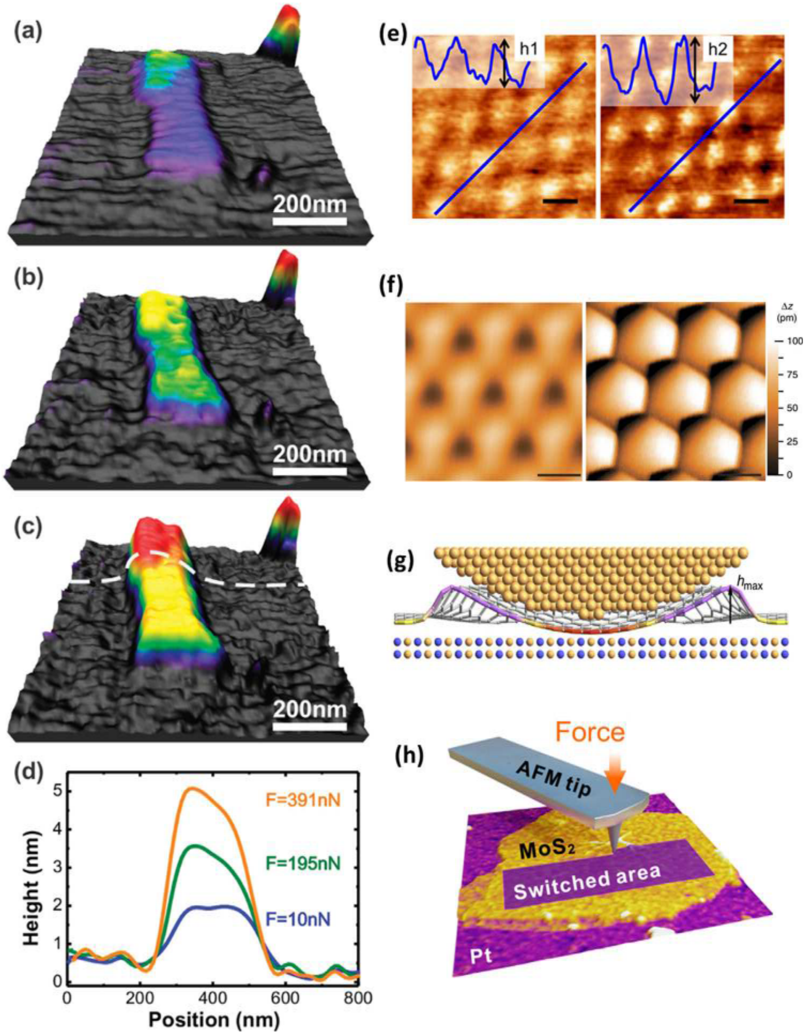

FIG. 11. SPM-based pressure-tuned properties of vdW materials. (a)–(c) Contact mode AFM images of the same graphene bilayer flake with increasing applied tip forces showing an apparent thickening (expansion) of graphene upon compression. Such giant negative compressibility is evidenced in the graph in panel (d). [(a)–(d)] Reprinted with permission from Barboza *et al.*, Nano Lett. **12**, 2313 (2012). Copyright 2012 American Chemical Society. (e) Effect of the AFM tip pressure on SiC-grown graphene morphology. Reproduced with permission from Meza *et al.*, Nanotechnology **26**, 255704 (2015). Copyright 2015 IOP Publishing. (f)–(g) A Similar effect of graphene tip-induced deformation is observed when graphene is placed atop h-BN, leading to different topographic patterns. Reproduced with permission from Yankowitz *et al.*, Nat. Commun. **7**, 13168 (2016). Copyright 2016 Authors, licensed under a Creative Commons Attribution. (h) Cartoon illustrating a piezoelectric domain switch of MoS_2 monolayers induced and controlled via the SPM tip. Reproduced with permission from Lipatov *et al.*, npj 2D Mater. Appl. **6**, 18 (2022). Copyright 2022 Authors, licensed under a Creative Commons Attribution.

stacking of graphene on h-BN [Figs. 11(f)–11(g)].[164] As illustrated in panel g, the pressure exerted by the STM tip deforms the monolayer graphene causing a significant variation on the observed topography [left and right images in Fig. 11(f)].[164] Finally, a recent study has shown the possibility of switching the out-of-plane polarization of MoS_2 via pressure application by an AFM tip.[165] As illustrated by the cartoon in Fig. 11(h), some piezoelectric properties can be tuned in desired patterns on a MoS_2 flake.[165]

V. MODELING ATOMICALLY THIN VAN DER WAALS MATERIALS AT HIGH PRESSURES

What makes a 2D pressure-induced phase transition and/or modulation of electronic properties special relative to its bulk counterpart? A first aspect, as pointed out by Kvashinin *et al.*,[166] concerns the central role played by surface chemistry in the 2D case, which may trigger structural phase transitions in relative smaller values of pressure. The covalent incorporation of other chemical species at the surface is, by itself, an important ingredient in the structural and electronic characterization of the resulting structure. A second aspect concerns the idiosyncrasies of layered compounds, which allows for electronic modulation by application of an in-plane strain or by a pressure-induced control of interlayer interactions. In the following, we shall use carbon and related materials to illustrate the first point and transition metal dichalcogenides and twisted layers to address the second. Prior to this discussion, we shall present the main theoretical approaches that have been employed to address the problem of the characterization of 2D nanostructures under pressure.

A. Methodology

From the methodological point of view, the problem of 2D nanostructures under pressure has been addressed by standard techniques, such as the Pseudopotential Density Functional Theory (DFT) formalism, the tight-binding method and molecular dynamics simulations. More subtle is the scheme adopted to simulate the application of pressure in a first principles approach. The vacuum region inherent to 2D models prevents, in principle, a straightforward implementation of pressure effects with constraints imposed on the components of the stress tensor. Fixing position of selected atoms may introduce unphysical ingredients to the problem. The issue has been circunvent with distinct approaches. To mimic the effect of uniaxial pressure in silicene layers, Tantardini *et al.*[167] has filled the vacuum region with helium layers. This scheme allows for a full relaxation of in-plane lattice vectors and do not involve any position constraint in the system. In another approach, the uniaxial pressure problem has been overcome by the adoption of the so-called "hard wall" constraints. As before, the method does not require any atom to be fixed. However, limits are imposed on the maximum and minimum values of the vertical components (along the z-axis) of atomic positions—the force component F_z is set to zero if it is positive and the z-component of the position is larger than a predefined upper limit, with analogous constraints imposed in the bottom region. The pressure is estimated by the remanent (or constrained) forces in one of the surfaces. The case of hydrostatic pressure can be addressed by a combination of schemes: in-plane pressure controlled by the constrained stress tensor, while vertical forces adjusted with the above method. Alternatively, in the case of flat surfaces, the vertical forces may be predefined as constraints in the upper atoms during the relaxation, while the hard wall scheme is kept only in the bottom surface.[76]

Temperature and layer thickness are also important variables. Kvashnin *et al.*,[166] for instance, determine the Gibbs free energy from DFT calculations, which allows for the construction of the phase diagram including pressure, temperature, and layer thickness. In this approach, the Gibbs potential, following the work of Kern *et al.*,[168] is given by

$$G(P,T) = E_0(V) + PV + U_0(V) + F_{vib}(T,V), \tag{7}$$

in which E_0 is the total energy, F_{vib} and U_0 are the vibrational and zero-point energies, respectively, and are determined in terms of the phonon density of states $g(V,\omega)$,

$$F_{vib} = k_B T \int_{\Omega} g(V,\omega) ln\left[1 - e^{-\frac{\hbar\omega}{k_B T}}\right] d\omega, \tag{8}$$

$$U_0(V) = \frac{1}{2}\int g(V,\omega)\hbar\omega d\omega. \tag{9}$$

Once the Gibbs potential is calculated, the temperature dependent phase transition pressure value can be determined.

B. Structural phase transitions

Few-layer graphene furnishes a good example of phase transition driven by pressure application. Indeed, if pressure is applied to a bilayer graphene in the presence of adsorbates, such as water vapor molecules, a concerted action may take place: (i) as a response to the pressure, the layers approach each other, which increases the sp^{3}character of the chemical bonding in the carbon system; (ii) the surface reactivity increases and the formation of –H and/or –OH radicals are facilitated in such scenario, resulting in the binding of chemical species in those atoms which would be left with unsaturated bonds in an all-sp^3 configuration; and (iii) a cooperative effect, driven by the geometric corrugation characteristic of the tetrahedral sp^3 bonds, propagates the reaction throughout the surface. The result may be a single-sided -H and/or –OH functionalized two-layer diamond-like structure, named diamondol (or graphone-like structure or diamondene), or a complete functionalized 2D-diamond, the diamane.

The former has been observed and characterized in scanning probe microscopy (SPM) experiments[72,79] and in pressure vessels coupled to Raman spectroscopy apparatus,[76] while the latter have been extensively investigated[68,79,169] since first theoretical proposals of analogue structures based on fluorinated graphene bilayers.[170] In fact, the role of surface chemistry is so important in such thin material that some authors report the synthesis of diamane under ambient conditions in experiments in which a hot filament provides -H radicals to interact with graphene.[171] Figures 12(a) and 12(b) show the relaxed DFT structures for both compounds.

Both, diamondol and diamane have been theoretically characterized by DFT calculations, which shows that the phase transition, estimated in the diamondol case to take place at P $\sim$10.0 GPa, is accompanied by strong modulation of electronic and mechanical properties. Diamane is a wide gap direct semiconductor. Diamondol—its single-sided counterpart—is a ferromagnetic semicondutor. This behavior is explained in terms of an array of unsaturated bonds left in the lower part of the structure. Each dangling bond possess a magnetic moment of 1 μ_B, within the DFT-GGA description, and a dispersive and spin polarized band shows up as the first conduction band. The energy gap assumes the value of 1.1 eV, considerably reduced compared to the diamane case. Figures 12(d) and 12(e) show band structures for diamane and diamondol, highlighting the low energy bands, which defines the gap region.

The diamondization of a bilayer graphene could be probed by the assessment of its mechanical properties: Does the transformed structure exhibits stiffness and hardness compatible with a diamond-like film? That was exactly the approach carried out by Gao *et al.*[73] to prove the sp^2 to sp^3 rehybridization. With calculations based on

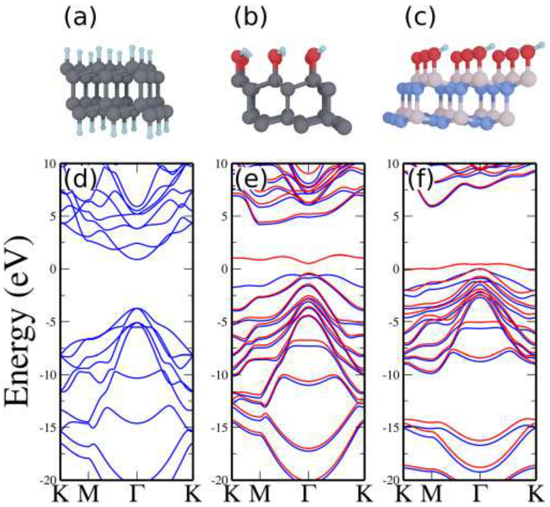

FIG. 12. Relaxed structures (a)–(c) and DFT-GGA band structures (d)–(e) for diamane, diamondol, and bonitrol, respectively, were calculated using the SIESTA software.[172–176] The Fermi level is set to zero in all plots. Diamane is a direct bandgap semiconductor (d), while diamondol is a ferromagnetic semiconductor (e). An array of unsaturated bonds left in the lower part of the structure confers two dispersive and spin-polarized bands to diamondol. Bonitrol, on the other hand, has a metallic behavior (f), with the defective band crossing the Fermi level. Both diamondol and bonitrol possess a magnetic moment of 1 B. Light cyan, red, gray, blue, and pink spheres represent H, O, C, N, and B atoms, respectively.

atomistic models combined with Hookean force fields, they were able to estimate force vs indentation depth curves in distinct scenarios. The comparison with experimental indentation curves strongly supported the phase transition hypothesis.

The sp^2-sp^3 rehybridization may propagate throughout the structure if more layers are available. In the diamondol case, it represents a top-bottom process, which requires increasing values of pressure. Here, the stacking order shows up as a new variable: in a few-layer graphene with AB stacking, the diamondization eventually requires layer sliding, which, interestingly, may lead to the stabilization (from the third layer, counting from the top surface, to the bottom of the structure) of a hexagonal diamond lonsdaleite-type stacking.[56] In principle, this agrees with calculations in graphite to diamond transitions, which indicates the important role of kinetics effects in favoring an initial nucleation mechanism for hexagonal diamond and its faster propagation growth.[177]

The phenomenology has also been observed in other 2D materials—hexagonal boron nitride (hBN) is the immediate example due to the chemical similarities between C–C and B–N bonds. In fact, it leads to similar structural features, but, obviously, with marked differences in the electronic aspects. In the hBN case, –OH radicals may bind to the upper boron atoms as the layers approach each other, promoting the restructuring and leaving an array of dangling bonds in the nitrogen atoms of the bottommost layer,[146] as shown in Fig. 12(c). Again, localized states are responsible for magnetic ordering and spin polarized bands, as it can be seen in Fig. 12(f). Due to the proximity of these unsatured bonds, the defective band is relatively dispersive and crosses the Fermi level, rendering metallic behavior to the resulting compound. The threshold pressure required to trigger the process has been estimated to be 7.0 GPa. In few-layer systems (up to seven layers), calculations suggest that pressure values of this order keeps the rehybridizaton restricted to the two top layers.On the top surface, N–H bonds may be formed instead of B–OH bonds, leaving the dangling bonds at the bottom side centered at boron sites. This configuration is thermodinamically less stable than the previous one, though. A complete diamondization of atomically thin hBN on top of SiO$_2$ substrate—a BN diamane analogue—has also been observed and characterized with spectroscopic and theoretical techniques[150] based on molecular dynamics simulations. The authors described its formation as induced by pressure with no need of chemical functionalizaton. The sp^2 to sp^3 conversion is accompanied by a stiffening phenomenon in the pressure range of 2.0–4.0 GPa for bi- and trilayers.

The question on reversibility has also been addressed. The experimental reports[72,150] suggests a reversible transformation. The theoretical treatments rationalize this trend in terms of functionalization coverage: above a critical coverage, ultra-thin diamond-like structures may become stable.[72]

How would be the behavior of 2D few-layer structures based on heavier elements? A systematic study conducted by Tantardini *et al.* on silicene layers shed light on this issue.[167] At zero pressure, silicene layers are corrugated, reflecting the predominance of a sp^3 hybrid orbitals in the chemical bonds. The availability of *d* orbitals in the third electronic shell is a second important distinction relative to the carbon case. Upon uniaxial pressure, it is energetically more favorable for the hybridization in bi- and trilayers in AA and AAA stackings to pass from sp^3 to sp^{3}d, rather than to sp^2. The characteristic geometry of sp^3 hybrids is a trigonal bipyramidal arrangement, which confers a flat configuration to the layers. Therefore, the geometry does not evolve following a diamondization process, as in the carbon case. A charge redistribution does occur, though, and suggests the use of silicene layers as field effect transistor pressure sensors. Flattening is estimated to take place at 15.0 and 2.0 GPa for tri- and bilayers, respectively. The monolayer also flattens under a 15.0 GPa uniaxial pressure but as a consequence of a sp^3 to sp^2 rehybridization.

C. Modulation of electronic properties

The case of transition metal dichalcogenides is illustrative of the role of pressure in changing electronic properties while keeping the overall crystal structure. The effect has been reported by several groups,[59,96,178–180] and an intuitive grasp of the phenomenon may be pursued by analyzing orbital contributions for the bands close to the gap region.[96] Indeed, the lowest conduction state in TMDs, such as MoS$_2$ and MoSe$_2$, is predominantly built upon contributions of Mo 4d$_{z^2}$ orbitals in the K point; From K to Q point, the band goes up in energy, reaches a local maximum and a second minimum at the Q point (a local one, 0.2 eV above that in the K point). At the Q point, the most important contributions come from the in-plane Mo orbitals 4d$_{x^2-y^2}$ and 4d$_{xy}$. This is illustrated in Fig. 4(h) for the MoS$_2$ case.

How are these features related to pressure effects in TMDs? An in-plane compression should have a larger effect in the states built upon the in-plane orbitals, those with predominant contributions in the Q point, and the net result would be a decrease in the energy of this state, which, eventually, would become lower in energy than the state in the K point. The prediction is, therefore, a direct to indirect bandgap transition and, eventually, a decrease in the gap value or even a semiconductor-metal transition. The K–Q crossover is indeed observed in photoluminesce measurements at a critical pressure of 1.9 GPa[96] and also in double-resonance Raman measurements.[59] Similar analyses have been reported for distinct types of tensile and shear strains, for both few-layer and monolayer TMDs.[178–180]

The changes in the electronic structure of TMDs due to variations in the interlayer distance is another example of the role of pressure in modulating the electronic behavior. The top of the valence band at the Γ point in TMDs [see Fig. 4(h) for the MoS_2 case] is dominated by Mo $4d_{z^2}$ and S $3p_z$ orbitals, which strongly respond to vertical compressive forces[159,180] moving up in energy, toward the Fermi level.

Pressure may also be an important variable in the growing field of twistronics. The large cells required to represent small-twisted angles—as the 1.1° magic angle, which leads to flatband phenomenology in bilayer graphene[12,109]—prevents the use of a first principles formalism. However, tight binding calculations[117] have been employed in this context, particularly in addressing the effects of pressure in modulating the emergence and energy position of flat bands. Carr *et al.*,[117] for instance, have used interlayer coupling parameters determined, as a function of pressure, by a quadratic fit; the pressure, in its turn, is given by a functional form of the type $P = A(e^{-B\epsilon} - 1)$, in which ϵ is related to the interlayer distance d ($\epsilon = 1 - d/d_0$), and A and B are adjustable parameters. Within this scheme, the pressure is shown to drive the emergence of flat bands in larger twist angles: under 9.2 GPa (10% compression), the magic angle increases to 2.0°. The results indicates that pressure is a fundamental ingredient in describing correlated states, which may have important consequences in the field of superconductivity.

VI. OUTLOOK

In this section, we discuss possible research directions in the field of high-pressure studies of atomically thin van der Waals systems within two different approaches: (i) high-pressure synthesis of novel 2D materials and (ii) pressure tuning of properties and many-body states of 2D materials and moiré heterostructures.

A. High-pressure synthesis of novel 2D materials

As discussed in Secs. II C and IV B, there has been compelling evidence for the high-pressure conversion of few-layer graphene to 2D diamond obtained either from SPM[72,73] or DAC experiments,[56,76–78] as well as evidence for the diamondization of hBN[146,150] and the formation of covalent bonds between graphene and hBN from SPM experiments.[147] Therefore, it would be highly insightful to obtain information about the new "hBN diamond" and hybrid "graphene-hBN" phases via spectroscopic or transport methods using DACs. For that purpose, the use of water PTM could be beneficial to drive and reduce the critical pressures necessary to start the phase transition.[56,76,181] Furthermore, water should also functionalize monolayer TMDs under compression,[159] leading to a metallic phase that could be characterized by a PL quenching and/or a change in the electrical resistance. Compression of twisted bilayer graphene could potentially lead to the formation of moiré 2D diamonds with different spin-localization configurations depending on the twist-angle.[182]

Another interesting approach that has been recently demonstrated is the high-pressure synthesis of new classes of 2D layered van der Waals materials from elemental compounds. Examples are the synthesis of pentagonal 2D NiN_2[183] and the Dirac material BeN_4[184] from high-pressure high-temperature (via laser heating) reaction between nickel and nitrogen, and beryllium and nitrogen, respectively.

B. Pressure tuning of properties and many-body states of 2D materials and moiré heterostructures

There is a vast range of physical properties of 2D materials and moiré heterostructures (electronic, vibrational, magnetic, etc.) that can be investigated via pressure tuning. One interesting direction is to investigate the layer-dependent magnetism as a function of pressure and temperature in novel 2D van der Waals magnets such as NiI_2.[185] These experiments can help unravel the interplay between stacking order, interlayer distance, and the number of layers in determining the magnetic ground state in these materials. Furthermore, NiI_2 is an example of a multiferroic, a class of materials featuring coupled ferroelectric and magnetic order that have garnered wide interest for their exceptional static and dynamical magnetoelectric properties.[186] Pressure may be an invaluable tool to tune and investigate the coupling between the magnetic and ferroelectric order in such atomically thin systems. The magnetic properties of vdW heterostructures such as $CrBr_3/CrI_3$ or WSe_2/CrI_3[187] can also be explored under pressure, enabling direct control of the exchange bias and other forms of magnetic proximity effects that depend strongly on the interlayer distance.

Regarding pressure tuning of many-body states, an exciting research avenue is the investigation of moiré excitons at high pressures. Moiré excitons consist in excitons confined to the local minima of the supperlattice potential in moiré system, working as an artificial lattice of interacting quasiparticles.[188] These excitations have been observed in several recent studies involving TMD heterostructures such as $MoSe_2/WSe_2$[189,190] and WSe_2/WS_2,[191] exhibiting an ultra-sharp photoluminescence signal as a characteristic signature. High pressure is a powerful tool to tune and investigate the interactions between moiré excitons by reducing the average quasiparticle distance and increasing the strength of the moiré potential, due to the in-plane compression and reduction of interlayer distance, respectively. The system could then be probed by photoluminescence spectroscopy and reflection contrast using DACs. There are also exciting open challenges in performing transport measurements of strongly correlated, superconducting, and topological moiré materials in DACs, affording the ability to apply substantially higher pressure than has been achieved in piston-cylinder cells so far. These experiments may help to uncover fundamentally new ground states that are inaccessible at ambient pressure.

In summary, the combination of high-pressure experiments and atomically thin van der Waals materials is a powerful one for both its scientific aspects, with a myriad of interesting phenomena, and its possible technological outcomes. There is a vast range of possibilities to be explored, and we hope this review may help the advancement of this research field.

ACKNOWLEDGMENTS

Work at MIT (L.G.P.M. and R.C.) was supported by the STC Center for Integrated Quantum Materials, NSF Grant No. DMR-1231319. M.Y. acknowledges the support of the Army Research Office under Grant No. W911NF-20–1-0211. M.J.S.M., M.S.C.M., and B.R.A.N. acknowledge financial support from CNPq, CAPES, FAPEMIG, and Brazilian Institute of Science and Technology (INCT) in Carbon Nanomaterials, Rede Mineira de Materiais Bidimensionais (FAPEMIG). M.J.S.M. acknowledges the support from Universidade Federal de Ouro Preto (UFOP).

AUTHOR DECLARATIONS

Conflict of Interest

The authors have no conflicts to disclose.

Author Contributions

Luiz Gustavo Pimenta Martins: Conceptualization (lead); Writing – original draft (equal); Writing – review & editing (equal). **Riccardo Comin:** Writing – original draft (equal); Writing – review & editing (equal). **Matheus J. S. Matos:** Writing – original draft (equal); Writing – review & editing (equal). **Mario S. C. Mazzoni:** Writing – original draft (equal); Writing – review & editing (equal). **Bernardo Ruegger Almeida Neves:** Writing – original draft (equal); Writing – review & editing (equal). **Matthew Yankowitz:** Writing – original draft (equal); Writing – review & editing (equal).

DATA AVAILABILITY

Data sharing is not applicable to this article as no new data were created or analyzed in this study.

REFERENCES

[1] K. S. Novoselov, D. Jiang, F. Schedin, T. Booth, V. Khotkevich, S. Morozov, and A. K. Geim, "Two-dimensional atomic crystals," Proc. Natl. Acad. Sci. U.S.A. **102**, 10451–10453 (2005).

[2] P. Ajayan, P. Kim, and K. Banerjee, "Two-dimensional van der Waals materials," Phys. Today **69**(9), 38 (2016).

[3] K. Novoselov, O. A. Mishchenko, O. A. Carvalho, and A. C. Neto, "2D materials and van der Waals heterostructures," Science **353**, aac9439 (2016).

[4] K. I. Bolotin, K. J. Sikes, J. Hone, H. Stormer, and P. Kim, "Temperature-dependent transport in suspended graphene," Phys. Rev. Lett. **101**, 096802 (2008).

[5] A. Taube, J. Judek, A. Łapińska, and M. Zdrojek, "Temperature-dependent thermal properties of supported MoS$_2$ monolayers," ACS Appl. Mater. Interfaces **7**, 5061–5065 (2015).

[6] A. Allain and A. Kis, "Electron and hole mobilities in single-layer WSe$_2$," ACS Nano **8**, 7180–7185 (2014).

[7] Y. Zhang, T.-T. Tang, C. Girit, Z. Hao, M. C. Martin, A. Zettl, M. F. Crommie, Y. R. Shen, and F. Wang, "Direct observation of a widely tunable bandgap in bilayer graphene," Nature **459**, 820–823 (2009).

[8] L. A. Jauregui, A. Y. Joe, K. Pistunova, D. S. Wild, A. A. High, Y. Zhou, G. Scuri, K. De Greve, A. Sushko, C.-H. Yu *et al.*, "Electrical control of interlayer exciton dynamics in atomically thin heterostructures," Science **366**, 870–875 (2019).

[9] Y. Tang, J. Gu, S. Liu, K. Watanabe, T. Taniguchi, J. Hone, K. F. Mak, and J. Shan, "Tuning layer-hybridized Moiré excitons by the quantum-confined stark effect," Nat. Nanotechnol. **16**, 52–57 (2021).

[10] S. Pisana, M. Lazzeri, C. Casiraghi, K. S. Novoselov, A. K. Geim, A. C. Ferrari, and F. Mauri, "Breakdown of the adiabatic Born–Oppenheimer approximation in graphene," Nat. Mater. **6**, 198–201 (2007).

[11] S. Mouri, Y. Miyauchi, and K. Matsuda, "Tunable photoluminescence of monolayer mos2 via chemical doping," Nano Lett. **13**, 5944–5948 (2013).

[12] Y. Cao, V. Fatemi, S. Fang, K. Watanabe, T. Taniguchi, E. Kaxiras, and P. Jarillo-Herrero, "Unconventional superconductivity in magic-angle graphene superlattices," Nature **556**, 43–50 (2018).

[13] Y. Tang, L. Li, T. Li, Y. Xu, S. Liu, K. Barmak, K. Watanabe, T. Taniguchi, A. H. MacDonald, J. Shan *et al.*, "Simulation of hubbard model physics in WSe$_2$/WS$_2$ Moiré superlattices," Nature **579**, 353–358 (2020).

[14] K. S. Burch, D. Mandrus, and J.-G. Park, "Magnetism in two-dimensional van der Waals materials," Nature **563**, 47–52 (2018).

[15] K. F. Mak, J. Shan, and D. C. Ralph, "Probing and controlling magnetic states in 2D layered magnetic materials," Nat. Rev. Phys. **1**, 646–661 (2019).

[16] Y. Wang, Y. Huang, Y. Song, X. Zhang, Y. Ma, J. Liang, and Y. Chen, "Room-temperature ferromagnetism of graphene," Nano Lett. **9**, 220–224 (2009).

[17] N. Levy, S. Burke, K. Meaker, M. Panlasigui, A. Zettl, F. Guinea, A. C. Neto, and M. F. Crommie, "Strain-induced pseudo–magnetic fields greater than 300 tesla in graphene nanobubbles," Science **329**, 544–547 (2010).

[18] C. Si, Z. Sun, and F. Liu, "Strain engineering of graphene: A review," Nanoscale **8**, 3207–3217 (2016).

[19] A. Castellanos-Gomez, R. Roldán, E. Cappelluti, M. Buscema, F. Guinea, H. S. van der Zant, and G. A. Steele, "Local strain engineering in atomically thin MoS$_2$," Nano Lett. **13**, 5361–5366 (2013).

[20] Y. Bai, L. Zhou, J. Wang, W. Wu, L. J. McGilly, D. Halbertal, C. F. B. Lo, F. Liu, J. Ardelean, P. Rivera *et al.*, "Excitons in strain-induced one-dimensional moiré potentials at transition metal dichalcogenide heterojunctions," Nat. Mater. **19**, 1068–1073 (2020).

[21] L. Zhang, Y. Tang, A. R. Khan, M. M. Hasan, P. Wang, H. Yan, T. Yildirim, J. F. Torres, G. P. Neupane, Y. Zhang *et al.*, "2D materials and heterostructures at extreme pressure," Adv. Sci. **7**, 2002697 (2020).

[22] S. Pei, Z. Wang, and J. Xia, "High pressure studies of 2D materials and heterostructures: A review," Mater. Des. **213**, 110363 (2021).

[23] J. E. Proctor, E. Gregoryanz, K. S. Novoselov, M. Lotya, J. N. Coleman, and M. P. Halsall, "High-pressure raman spectroscopy of graphene," Phys. Rev. B **80**, 073408 (2009).

[24] K. Filintoglou, N. Papadopoulos, J. Arvanitidis, D. Christofilos, O. Frank, M. Kalbac, J. Parthenios, G. Kalosakas, C. Galiotis, and K. Papagelis, "Raman spectroscopy of graphene at high pressure: Effects of the substrate and the pressure transmitting media," Phys. Rev. B **88**, 045418 (2013).

[25] D. Machon, C. Bousige, R. Alencar, A. Torres-Dias, F. Balima, J. Nicolle, G. de Sousa Pinheiro, A. G. Souza Filho, and A. San-Miguel, "Raman scattering studies of graphene under high pressure," J. Raman Spectrosc. **49**, 121–129 (2018).

[26] See https://www.nobelprize.org/prizes/physics/1946/summary for "Nobel Prize Outreach AB" (accessed January 24, 2022).

[27] A. Jayaraman, "Diamond anvil cell and high-pressure physical investigations," Rev. Mod. Phys. **55**, 65 (1983).

[28] W. A. Bassett, "Diamond anvil cell, 50th birthday," High Pressure Res. **29**, 163–186 (2009).

[29] B. Li, C. Ji, W. Yang, J. Wang, K. Yang, R. Xu, W. Liu, Z. Cai, J. Chen, and H.-k. Mao, "Diamond anvil cell behavior up to 4 mbar," Proc. Natl. Acad. Sci. U. S. A. **115**, 1713–1717 (2018).

[30] A. Dewaele, P. Loubeyre, F. Occelli, O. Marie, and M. Mezouar, "Toroidal diamond anvil cell for detailed measurements under extreme static pressures," Nat. Commun. **9**, 2913 (2018).

[31] M. P. Pasternak, R. D. Taylor, A. Chen, C. Meade, L. Falicov, A. Giesekus, R. Jeanloz, and Y. Y. Peter, "Pressure-induced metallization and the collapse of the magnetic state in the antiferromagnetic insulator NiI$_2$," Phys. Rev. Lett. **65**, 790 (1990).

[32] R. Reichlin, K. E. Brister, A. K. McMahan, M. Ross, S. Martin, Y. K. Vohra, and A. L. Ruoff, "Evidence for the insulator-metal transition in xenon from optical, x-ray, and band-structure studies to 170 GPa," Phys. Rev. Lett. **62**, 669 (1989).

[33] T. Yagi, W. Utsumi, M-a Yamakata, T. Kikegawa, and O. Shimomura, "High-pressure in situ x-ray-diffraction study of the phase transformation from graphite to hexagonal diamond at room temperature," Phys. Rev. B **46**, 6031 (1992).

[34] H. Xia, S. J. Duclos, A. L. Ruoff, and Y. K. Vohra, "New high-pressure phase transition in zirconium metal," Phys. Rev. Lett. **64**, 204 (1990).

[35] R. Jaramillo, Y. Feng, J. Lang, Z. Islam, G. Srajer, P. Littlewood, D. McWhan, and T. Rosenbaum, "Breakdown of the Bardeen–Cooper–Schrieffer ground state at a quantum phase transition," Nature **459**, 405–409 (2009).

[36] Y. Wang, T. Rosenbaum, A. Palmer, Y. Ren, J.-W. Kim, D. Mandrus, and Y. Feng, "Strongly-coupled quantum critical point in an all-in-all-out antiferromagnet," Nat. Commun. **9**, 2953 (2018).

[37] A. Drozdov, M. Eremets, I. Troyan, V. Ksenofontov, and S. I. Shylin, "Conventional superconductivity at 203 kelvin at high pressures in the sulfur hydride system," Nature **525**, 73–76 (2015).

[38] J. A. Flores-Livas, L. Boeri, A. Sanna, G. Profeta, R. Arita, and M. Eremets, "A perspective on conventional high-temperature superconductors at high pressure: Methods and materials," Phys. Rep. **856**, 1–78 (2020).

[39] L. Zhang, Y. Wang, J. Lv, and Y. Ma, "Materials discovery at high pressures," Nat. Rev. Mater. **2**, 1–16 (2017).

[40] P. F. McMillan, "New materials from high-pressure experiments," Nat. Mater. **1**, 19–25 (2002).

[41] W. Zhang, A. R. Oganov, A. F. Goncharov, Q. Zhu, S. E. Boulfelfel, A. O. Lyakhov, E. Stavrou, M. Somayazulu, V. B. Prakapenka, and Z. Konôpková, "Unexpected stable stoichiometries of sodium chlorides," Science **342**, 1502–1505 (2013).

[42] E. Horvath-Bordon, R. Riedel, A. Zerr, P. F. McMillan, G. Auffermann, Y. Prots, W. Bronger, R. Kniep, and P. Kroll, "High-pressure chemistry of nitride-based materials," Chem. Soc. Rev. **35**, 987–1014 (2006).

[43] I. Spain and D. Dunstan, "The technology of diamond anvil high-pressure cells: II. Operation and use," J. Phys. E **22**, 923 (1989).

[44] H. Mao, P. Bell, J. t Shaner, and D. Steinberg, "Specific volume measurements of Cu, Mo, Pd, and Ag and calibration of the ruby R_1 fluorescence pressure Gauge from 0.06 to 1 mbar," J. Appl. Phys. **49**, 3276–3283 (1978).

[45] H. Mao, J.-A. Xu, and P. Bell, "Calibration of the ruby pressure gauge to 800 kbar under quasi-hydrostatic conditions," J. Geophys. Res. **91**, 4673–4676, https://doi.org/10.1029/JB091iB05p04673 (1986).

[46] M. Hanfland and K. Syassen, "A Raman study of diamond anvils under stress," J. Appl. Phys. **57**, 2752–2756 (1985).

[47] W. Holzapfel, M. Hartwig, and W. Sievers, "Equations of state for Cu, Ag, and Au for wide ranges in temperature and pressure up to 500 GPa and above," J. Phys. Chem. Ref. Data **30**, 515–529 (2001).

[48] K. Syassen, "Ruby under pressure," High Pressure Res. **28**, 75–126 (2008).

[49] H. Yamaoka, Y. Zekko, I. Jarrige, J.-F. Lin, N. Hiraoka, H. Ishii, K.-D. Tsuei, and J. Mizuki, "Ruby pressure scale in a low-temperature diamond anvil cell," J. Appl. Phys. **112**, 124503 (2012).

[50] D. D. Ragan, R. Gustavsen, and D. Schiferl, "Calibration of the ruby R_1 and R_2 fluorescence shifts as a function of temperature from 0 to 600 k," J. Appl. Phys. **72**, 5539–5544 (1992).

[51] H. Lee, E. Park, T. Park, V. Sidorov, F. Ronning, E. Bauer, and J. Thompson, "Pressure-induced superconducting state of antiferromagnetic CaFe$_2$ As$_2$," Phys. Rev. B **80**, 024519 (2009).

[52] G. Piermarini, S. Block, and J. Barnett, "Hydrostatic limits in liquids and solids to 100 kbar," J. Appl. Phys. **44**, 5377–5382 (1973).

[53] N. Tateiwa and Y. Haga, "Evaluations of pressure-transmitting media for cryogenic experiments with diamond anvil cell," Rev. Sci. Instrum. **80**, 123901 (2009).

[54] B. Olinger and P. M. Halleck, "Compression and bonding of ice VII and an empirical linear expression for the isothermal compression of solids," J. Chem. Phys **62**, 94–99 (1975).

[55] E. Wolanin, P. Pruzan, J. Chervin, B. Canny, M. Gauthier, D. Häusermann, and M. Hanfland, "Equation of state of ice VII up to 106 GPa," Phys. Rev. B **56**, 5781 (1997).

[56] L. G. Pimenta Martins, D. L. Silva, J. S. Smith, A.-Y. Lu, C. Su, M. Hempel, C. Occhialini, X. Ji, R. Pablo, R. S. Alencar *et al.*, "Hard, transparent, sp^3-containing 2D phase formed from few-layer graphene under compression," Carbon **173**, 744–757 (2021).

[57] S. Klotz, J. Chervin, P. Munsch, and G. Le Marchand, "Hydrostatic limits of 11 pressure transmitting media," J. Phys. D **42**, 075413 (2009).

[58] Y. Sun, W. Liu, I. Hernandez, J. Gonzalez, F. Rodriguez, D. Dunstan, and C. Humphreys, "3D strain in 2D materials: To what extent is monolayer graphene graphite?," Phys. Rev. Lett. **123**, 135501 (2019).

[59] L. G. Pimenta Martins, B. R. Carvalho, C. A. Occhialini, N. P. Neme, J.-H. Park, Q. Song, P. Venezuela, M. S. Mazzoni, M. J. Matos, J. Kong *et al.*, "Electronic band tuning and multivalley raman scattering in monolayer transition metal dichalcogenides at high pressures," ACS Nano **16**, 8064–8075 (2022).

[60] J. Nicolle, D. Machon, P. Poncharal, O. Pierre-Louis, and A. San-Miguel, "Pressure-mediated doping in graphene," Nano Lett. **11**, 3564–3568 (2011).

[61] A. Jorio, M. S. Dresselhaus, R. Saito, and G. Dresselhaus, *Raman Spectroscopy in Graphene Related Systems* (John Wiley & Sons, 2010).

[62] M. M. Cardona and G. Güntherodt, "Light scattering in solids IV," Top. Appl. Phys. **54**, 467 (1984).

[63] T. Mohiuddin, A. Lombardo, R. Nair, A. Bonetti, G. Savini, R. Jalil, N. Bonini, D. Basko, C. Galiotis, N. Marzari *et al.*, "Uniaxial strain in graphene by Raman spectroscopy: G peak splitting, grüneisen parameters, and sample orientation," Phys. Rev. B **79**, 205433 (2009).

[64] J. E. Lee, G. Ahn, J. Shim, Y. S. Lee, and S. Ryu, "Optical separation of mechanical strain from charge doping in graphene," Nat. Commun. **3**, 1024 (2012).

[65] A. Das, S. Pisana, B. Chakraborty, S. Piscanec, S. K. Saha, U. V. Waghmare, K. S. Novoselov, H. R. Krishnamurthy, A. K. Geim, A. C. Ferrari *et al.*, "Monitoring dopants by raman scattering in an electrochemically top-gated graphene transistor," Nat. Nanotechnol. **3**, 210–215 (2008).

[66] Y. Feng, R. Jaramillo, J. Wang, Y. Ren, and T. Rosenbaum, "Invited article: High-pressure techniques for condensed matter physics at low temperature," Rev. Sci. Instrum. **81**, 041301 (2010).

[67] K. S. Novoselov, A. K. Geim, S. Morozov, D. Jiang, Y. Zhang, S. Dubonos, I. Grigorieva, and A. Firsov, "Electric field effect in atomically thin carbon films," Science **306**, 666–669 (2004).

[68] P. B. Sorokin and B. I. Yakobson, "Two-dimensional diamond–diamane: Current state and further prospects," Nano Lett. **21**, 5475–5484 (2021).

[69] F. Piazza, K. Gough, M. Monthioux, P. Puech, I. Gerber, R. Wiens, G. Paredes, and C. Ozoria, "Low temperature, pressureless sp^2 to sp^3 transformation of ultrathin, crystalline carbon films," Carbon **145**, 10–22 (2019).

[70] F. Piazza, M. Monthioux, P. Puech, and I. C. Gerber, "Towards a better understanding of the structure of diamanoïds and diamanoïd/graphene hybrids," Carbon **156**, 234–241 (2020).

[71] P. V. Bakharev, M. Huang, M. Saxena, S. W. Lee, S. H. Joo, S. O. Park, J. Dong, D. C. Camacho-Mojica, S. Jin, Y. Kwon *et al.*, "Chemically induced transformation of chemical vapour deposition grown bilayer graphene into fluorinated single-layer diamond," Nat. Nanotechnol. **15**, 59–66 (2020).

[72] A. P. Barboza, M. H. Guimaraes, D. V. Massote, L. C. Campos, N. M. Barbosa Neto, L. G. Cancado, R. G. Lacerda, H. Chacham, M. S. Mazzoni, and B. R. Neves, "Room-temperature compression-induced diamondization of few-layer graphene," Adv. Mater. **23**, 3014–3017 (2011).

[73] Y. Gao, T. Cao, F. Cellini, C. Berger, W. A. De Heer, E. Tosatti, E. Riedo, and A. Bongiorno, "Ultrahard carbon film from epitaxial two-layer graphene," Nat. Nanotechnol. **13**, 133 (2018).

[74] F. Cellini, F. Lavini, T. Cao, W. de Heer, C. Berger, A. Bongiorno, and E. Riedo, "Epitaxial two-layer graphene under pressure: Diamene stiffer than diamond," FlatChem **10**, 8–13 (2018).

[75] F. Cellini, F. Lavini, C. Berger, W. De Heer, and E. Riedo, "Layer dependence of graphene-diamene phase transition in epitaxial and exfoliated few-layer graphene using machine learning," 2D Mater. **6**, 035043 (2019).

[76] L. G. Pimenta, M. J. S. Matos, A. R. Paschoal, P. T. C. Freire, N. F. Andrade, A. L. Aguiar, J. Kong, B. R. A. Neves, A. B. de Oliveira, M. S. C. Mazzoni, A. G. S. Filho, and L. G. Cançado, "Raman evidence for pressure-induced formation of diamondene," Nat. Commun. **8**, 96 (2017).

[77] F. Ke, Y. Chen, K. Yin, J. Yan, H. Zhang, Z. Liu, J. S. Tse, J. Wu, H-k Mao, and B. Chen, "Large bandgap of pressurized trilayer graphene," Proc. Natl. Acad. Sci. U. S. A. **116**, 9186–9190 (2019).

[78] F. Ke, L. Zhang, Y. Chen, K. Yin, C. Wang, Y.-K. Tzeng, Y. Lin, H. Dong, Z. Liu, J. S. Tse *et al.*, "Synthesis of atomically thin hexagonal diamond with compression," Nano Lett. **20**, 5916–5921 (2020).

[79] F. Lavini, M. Rejhon, and E. Riedo, "Two-dimensional diamonds from sp^2-to-sp^3 phase transitions," Nat. Rev. Mater. **7**, 814–832 (2022).

[80] M. Hanfland, H. Beister, and K. Syassen, "Graphite under pressure: Equation of state and first-order raman modes," Phys. Rev. B **39**, 12598 (1989).

[81] M. Hanfland, K. Syassen, and R. Sonnenschein, "Optical reflectivity of graphite under pressure," Phys. Rev. B **40**, 1951 (1989).

[82] R. Aust and H. Drickamer, "Carbon: A new crystalline phase," Science **140**, 817–819 (1963).

[83] W. L. Mao, H.-K. Mao, P. J. Eng, T. P. Trainor, M. Newville, C.-C. Kao, D. L. Heinz, J. Shu, Y. Meng, and R. J. Hemley, "Bonding changes in compressed superhard graphite," Science **302**, 425–427 (2003).

[84] Q. Li, Y. Ma, A. R. Oganov, H. Wang, H. Wang, Y. Xu, T. Cui, H.-K. Mao, and G. Zou, "Superhard monoclinic polymorph of carbon," Phys. Rev. Lett. **102**, 175506 (2009).

[85] K. Umemoto, R. M. Wentzcovitch, S. Saito, and T. Miyake, "Body-centered tetragonal C_4: A viable sp^3 carbon allotrope," Phys. Rev. Lett. **104**, 125504 (2010).

[86] J.-T. Wang, C. Chen, and Y. Kawazoe, "Low-temperature phase transformation from graphite to sp^3 orthorhombic carbon," Phys. Rev. Lett. **106**, 075501 (2011).

[87] A. C. Ferrari and J. Robertson, "Resonant Raman spectroscopy of disordered, amorphous, and diamondlike carbon," Phys. Rev. B **64**, 075414 (2001).

[88] W. L. Marshall and E. Franck, "Ion product of water substance, 0–1000 °C, 1–10,000 bars new international formulation and its background," J. Phys. Chem. Ref. data **10**, 295–304 (1981).

[89] K. Vasu, E. Prestat, J. Abraham, J. Dix, R. Kashtiban, J. Beheshtian, J. Sloan, P. Carbone, M. Neek-Amal, S. Haigh *et al.*, "Van der waals pressure and its effect on trapped interlayer molecules," Nat. Commun. **7**, 12168 (2016).

[90] D. L. Silva, J. L. E. Campos, T. F. Fernandes, J. N. Rocha, L. R. Machado, E. M. Soares, D. R. Miquita, H. Miranda, C. Rabelo, O. P. V. Neto *et al.*, "Raman spectroscopy analysis of number of layers in mass-produced graphene flakes," Carbon **161**, 181–189 (2020).

[91] M. Amsler, J. A. Flores-Livas, L. Lehtovaara, F. Balima, S. A. Ghasemi, D. Machon, S. Pailhès, A. Willand, D. Caliste, S. Botti *et al.*, "Crystal structure of cold compressed graphite," Phys. Rev. Lett. **108**, 065501 (2012).

[92] Y. Wang, J. E. Panzik, B. Kiefer, and K. K. Lee, "Crystal structure of graphite under room-temperature compression and decompression," Sci. Rep. **2**, 520 (2012).

[93] E. M. Ferreira, M. V. Moutinho, F. Stavale, M. Lucchese, R. B. Capaz, C. Achete, and A. Jorio, "Evolution of the raman spectra from single-, few-, and many-layer graphene with increasing disorder," Phys. Rev. B **82**, 125429 (2010).

[94] E. Piatti, D. De Fazio, D. Daghero, S. R. Tamalampudi, D. Yoon, A. C. Ferrari, and R. S. Gonnelli, "Multi-valley superconductivity in ion-gated MoS_2 layers," Nano Lett. **18**, 4821–4830 (2018).

[95] A. P. Nayak, T. Pandey, D. Voiry, J. Liu, S. T. Moran, A. Sharma, C. Tan, C.-H. Chen, L.-J. Li, M. Chhowalla *et al.*, "Pressure-dependent optical and vibrational properties of monolayer molybdenum disulfide," Nano Lett. **15**, 346–353 (2015).

[96] L. Fu, Y. Wan, N. Tang, Y.-M. Ding, J. Gao, J. Yu, H. Guan, K. Zhang, W. Wang, C. Zhang *et al.*, "K-λ crossover transition in the conduction band of monolayer MoS_2 under hydrostatic pressure," Sci. Adv. **3**, e1700162 (2017).

[97] Y. Ye, X. Dou, K. Ding, D. Jiang, F. Yang, and B. Sun, "Pressure-induced k–λ crossing in monolayer WSe_2," Nanoscale **8**, 10843–10848 (2016).

[98] G. Li, A. Goni, K. Syassen, O. Brandt, and K. Ploog, "State mixing in InAs/GaAs quantum dots at the pressure-induced γ-x crossing," Phys. Rev. B **50**, 18420 (1994).

[99] A. Kormányos, G. Burkard, M. Gmitra, J. Fabian, V. Zólyomi, N. D. Drummond, and V. Fal'ko, "k× p theory for two-dimensional transition metal dichalcogenide semiconductors," 2D Mater. **2**, 022001 (2015).

[100] J. Xia, J. Yan, Z. Wang, Y. He, Y. Gong, W. Chen, T. C. Sum, Z. Liu, P. M. Ajayan, and Z. Shen, "Strong coupling and pressure engineering in WSe_2–$MoSe_2$ heterobilayers," Nat. Phys. **17**, 92–98 (2021).

[101] C. A. Parsons, "VIII. Experiments on carbon at high temperatures and under great pressures, and in contact with other substances," Proc. R. Soc. London **44**, 320–323 (1888).

[102] M. Yankowitz, J. Jung, E. Laksono, N. Leconte, B. L. Chittari, K. Watanabe, T. Taniguchi, S. Adam, D. Graf, and C. R. Dean, "Dynamic band-structure tuning of graphene Moiré superlattices with pressure," Nature **557**, 404–408 (2018).

[103] B. Fülöp, A. Márffy, E. Tóvári, M. Kedves, S. Zihlmann, D. Indolese, Z. Kovács-Krausz, K. Watanabe, T. Taniguchi, C. Schönenberger, I. Kézsmárki, P. Makk, and S. Csonka, "New method of transport measurements on van der Waals heterostructures under pressure," J. Appl. Phys. **130**, 064303 (2021).

[104] O. L. Blakslee, D. G. Proctor, E. J. Seldin, G. B. Spence, and T. Weng, "Elastic constants of compression–annealed pyrolytic graphite," J. Appl. Phys. **41**, 3373 (1970).

[105] G. Li, A. Luican, J. M. B. Lopes dos Santos, A. H. Castro Neto, A. Reina, J. Kong, and E. Y. Andrei, "Observation of van Hove singularities in twisted graphene layers," Nat. Phys. **6**, 109–113 (2010).

[106] J. Xue, J. Sanchez-Yamagishi, D. Bulmash, P. Jacquod, A. Deshpande, K. Watanabe, T. Taniguchi, P. Jarillo-Herrero, and B. J. LeRoy, "Scanning tunnelling microscopy and spectroscopy of ultra-flat graphene on hexagonal boron nitride," Nat. Mater. **10**, 282–285 (2011).

[107] R. Decker, Y. Wang, V. W. Brar, W. Regan, H.-Z. Tsai, Q. Wu, W. Gannett, A. Zettl, and M. F. Crommie, "Local electronic properties of graphene on a bn substrate via scanning tunneling microscopy," Nano Lett. **11**, 2291–2295 (2011).

[108] M. Yankowitz, J. Xue, D. Cormode, J. D. Sanchez-Yamagishi, K. Watanabe, T. Taniguchi, P. Jarillo-Herrero, P. Jacquod, and B. J. LeRoy, "Emergence of superlattice Dirac points in graphene on hexagonal boron nitride," Nat. Phys. **8**, 382–386 (2012).

[109] Y. Cao, V. Fatemi, A. Demir, S. Fang, S. L. Tomarken, J. Y. Luo, J. D. Sanchez-Yamagishi, K. Watanabe, T. Taniguchi, E. Kaxiras, R. C. Ashoori, and P. Jarillo-Herrero, "Correlated insulator behaviour at half-filling in magic-angle graphene superlattices," Nature **556**, 80–84 (2018).

[110] L. A. Ponomarenko, R. V. Gorbachev, G. L. Yu, D. C. Elias, R. Jalil, A. A. Patel, A. Mishchenko, A. S. Mayorov, C. R. Woods, J. R. Wallbank, M. Mucha-Kruczynski, B. A. Pio, M. Potemski, I. V. Grigorieva, K. S. Novoselov, F. Guinea, V. I. Fal'ko, and A. K. Geim, "Cloning of Dirac fermions in graphene superlattices," Nature **497**, 594–597 (2013).

[111] R. Ribeiro-Palau, C. Zhang, K. Watanabe, T. Taniguchi, J. Hone, and C. R. Dean, "Twistable electronics with dynamically rotatable heterostructures," Science **361**, 690–693 (2018).

[112] N. R. Finney, M. Yankowitz, L. Muraleetharan, K. Watanabe, T. Taniguchi, C. R. Dean, and J. Hone, "Tunable crystal symmetry in graphene–boron nitride heterostructures with coexisting Moiré superlattices," Nat. Nanotechnol. **14**, 1029–1034 (2019).

[113] B. Hunt, J. D. Sanchez-Yamagishi, A. F. Young, M. Yankowitz, B. J. LeRoy, K. Watanabe, T. Taniguchi, P. Moon, M. Koshino, P. Jarillo-Herrero, and R. C. Ashoori, "Massive Dirac fermions and Hofstadter butterfly in a van der Waals heterostructure," Science **340**, 1427–1430 (2013).

[114] C. R. Dean, L. Wang, P. Maher, C. Forsythe, F. Ghahari, Y. Gao, J. Katoch, M. Ishigami, P. Moon, M. Koshino, T. Taniguchi, K. Watanabe, K. L. Shepard, J. Hone, and P. Kim, "Hofstadter's butterfly and the fractal quantum Hall effect in Moire superlattices," Nature **497**, 598–602 (2013).

[115] L. Balents, C. R. Dean, D. K. Efetov, and A. F. Young, "Superconductivity and strong correlations in Moiré flat bands," Nat. Phys. **16**, 725–733 (2020).

[116] E. Y. Andrei and A. H. MacDonald, "Graphene bilayers with a twist," Nat. Mater. **19**, 1265–1275 (2020).

[117] S. Carr, S. Fang, P. Jarillo-Herrero, and E. Kaxiras, "Pressure dependence of the magic twist angle in graphene superlattices," Phys. Rev. B **98**, 085144 (2018).

[118] B. L. Chittari, N. Leconte, S. Javvaji, and J. Jung, "Pressure induced compression of flatbands in twisted bilayer graphene," Electron. Struct. **1**, 015001 (2019).

[119] C. Shen, Y. Chu, Q. Wu, N. Li, S. Wang, Y. Zhao, J. Tang, J. Liu, J. Tian, K. Watanabe, T. Taniguchi, R. Yang, Z. Y. Meng, D. Shi, O. V. Yazyev, and G. Zhang, "Correlated states in twisted double bilayer graphene," Nat. Phys. **16**, 520–525 (2020).

[120] X. Liu, Z. Hao, E. Khalaf, J. Y. Lee, K. Watanabe, T. Taniguchi, A. Vishwanath, and P. Kim, "Tunable spin-polarized correlated states in twisted double bilayer graphene," Nature **583**, 221–225 (2020).

[121] Y. Cao, D. Rodan-Legrain, O. Rubies-Bigorda, J. M. Park, K. Watanabe, T. Taniguchi, and P. Jarillo-Herrero, "Tunable correlated states and spin-polarized phases in twisted bilayer–bilayer graphene," Nature **583**, 215–220 (2020).

[122] G. W. Burg, J. Zhu, T. Taniguchi, K. Watanabe, A. H. MacDoinald, and E. Tutuc, "Correlated insulating states in twisted double bilayer graphene," Phys. Rev. Lett. **123**, 197702 (2019).

[123] M. He, Y. Li, J. Cai, Y. Liu, K. Watanabe, T. Taniguchi, X. Xu, and M. Yankowitz, "Symmetry breaking in twisted double bilayer graphene," Nat. Phys. **17**, 26–30 (2021).

[124] B. Szentpéeri, P. Rickhaus, F. K. de Vries, A. Márffy, B. Fülöp, E. Tóvári, K. Watanabe, T. Taniguchi, A. Kormanyos, S. Csonka, and P. Makk, "Tailoring the band structure of twisted double bilayer graphene with pressure," Nano Lett. **21**, 8777 (2021).

[125] C. Gong, L. Li, Z. Li, H. Ji, A. Stern, Y. Xia, T. Cao, W. Bao, C. Wang, Y. Wang, Z. Q. Qiu, R. J. Cava, S. G. Louie, J. Xia, and X. Zhang, "Discovery of intrinsic ferromagnetism in two-dimensional van der Waals crystals," Nature **546**, 265–269 (2017).

[126] B. Huang, G. Clark, E. Navarro-Moratalla, D. R. Klein, R. Cheng, K. L. Seyler, D. Zhong, E. Schmidgall, M. A. McGuire, D. H. Cobden, W. Yao, D. Xiao, P. Jarillo-Herrero, and X. Xu, "Layer-dependent ferromagnetism in a van der Waals crystal down to the monolayer limit," Nature **546**, 270–273 (2017).

[127] T. Song, X. Cai, M. W.-Y. Tu, X. Zhang, B. Huang, N. P. Wilson, K. L. Seyler, L. Zhu, T. Taniguchi, K. Watanabe, M. A. McGuire, D. H. Cobden, D. Xiao, W. Yao, and X. Xu, "Giant tunneling magnetoresistance in spin-filter van der Waals heterostructures," Science **360**, 1214–1218 (2018).

[128] D. R. Klein, D. MacNeill, J. L. Lado, D. Soriano, E. Navarro-Moratalla, K. Watanabe, T. Taniguchi, S. Manni, P. Canfield, J. Fernandez-Rossier, and P. Jarillo-Herrero, "Probing magnetism in 2D van der Waals crystalline insulators via electron tunneling," Science **360**, 1218–1222 (2018).

[129] M. A. McGuire, H. Dixit, V. R. Cooper, and B. C. Sales, "Coupling of crystal structure and magnetism in the layered, ferromagnetic insulator CrI$_3$," Chem. Mater. **27**, 612–620 (2014).

[130] Z. Sun, Y. Yi, T. Song, G. Clark, B. Huang, Y. Shan, S. Wu, D. Huang, C. Gao, Z. Chen, M. McGuire, T. Cao, D. Xiao, W.-T. Liu, W. Yao, X. Xu, and S. Wu, "Giant nonreciprocal second-harmonic generation from antiferromagnetic bilayer CrI$_3$," Nature **572**, 497–501 (2019).

[131] T. Song, Z. Fei, M. Yankowitz, Z. Lin, Q. Jiang, K. Hwangbo, Q. Zhang, B. Sun, T. Taniguchi, K. Watanabe, M. A. McGuire, D. Graf, T. Cao, J.-H. Chu, D. H. Cobden, C. R. Dean, D. Xiao, and X. Xu, "Switching 2D magnetic states via pressure tuning of layer stacking," Nat. Mater. **18**, 1298–1302 (2019).

[132] T. Li, S. Jiang, N. Sivadas, Z. Wang, Y. Xu, D. Weber, J. E. Goldberger, K. Watanabe, T. Taniguchi, C. J. Fennie, K. F. Mak, and J. Shan, "Pressure-controlled interlayer magnetism in atomically thin CrI$_3$," Nat. Mater. **18**, 1303–1308 (2019).

[133] A. K. Geim and I. V. Grigorieva, "Van der waals heterostructures," Nature **499**, 419–425 (2013).

[134] A. Avsar, J. Y. Tan, T. Taychatanapat, J. Balakrishnan, G. K. W. Koon, Y. Yeo, J. Lahiri, A. Carvalho, A. S. Rodin, E. C. T. O'Farrell, G. Eda, A. H. Castro Neto, and B. Özyilmaz, "Spin–orbit proximity effect in graphene," Nat. Commun. **5**, 4875 (2014).

[135] Z. Wang, D.-K. Ki, H. Chen, H. Berger, A. H. MacDonald, and A. F. Morpurgo, "Strong interface-induced spin–orbit interaction in graphene on WS$_2$," Nat. Commun. **6**, 8339 (2015).

[136] Z. Wang, D.-K. Ki, J. Y. Khoo, D. Mauro, H. Berger, L. S. Levitov, and A. F. Morpurgo, "Origin and magnitude of 'designer' spin-orbit interaction in graphene on semiconducting transition metal dichalcogenides," Phys. Rev. X **6**, 041020 (2016).

[137] B. Yang, M.-F. Tu, J. Kim, Y. Wu, H. Wang, J. Alicea, R. Wu, M. Bockrath, and J. Shi, "Tunable spin–orbit coupling and symmetry-protected edge states in graphene/WS$_2$," 2D Mater. **3**, 031012 (2016).

[138] B. Yang, M. Lohmann, D. Barroso, I. Liao, Z. Lin, Y. Liu, L. Bartels, K. Watanabe, T. Taniguchi, and J. Shi, "Strong electron-hole symmetric Rashba spin-orbit coupling in graphene/monolayer transition metal dichalcogenide heterostructures," Phys. Rev. B **96**, 041409(R) (2017).

[139] J. O. Island, X. Cui, C. Lewandowski, J. Y. Khoo, E. M. Spanton, H. Zhou, D. Rhodes, J. C. Hone, T. Taniguchi, K. Watanabe, L. S. Levitov, M. P. Zaletel, and A. F. Young, "Spin–orbit-driven band inversion in bilayer graphene by the van der Waals proximity effect," Nature **571**, 85–89 (2019).

[140] B. Fülöp, A. Márffy, S. Zihlmann, M. Gmitra, E. Tóvári, B. Szentpéeri, M. Kedves, K. Watanabe, T. Taniguchi, J. Fabian, C. Schönenberger, P. Makk, and S. Csonka, "Boosting proximity spin–orbit coupling in graphene/wse$_2$ heterostructures via hydrostatic pressure," npj 2D Mater. Appl. **5**, 82 (2021).

[141] D. Bonnell, *Scanning Probe Microscopy and Spectroscopy* (Wiley-VCH, New York, NY, 2001).

[142] A. Renger and K. Johnson, *Contact Mechanics* (Cambridge University Press, Cambridge, UK, 1985).

[143] F. Cellini, Y. Gao, and E. Riedo, "Å-indentation for non-destructive elastic moduli measurements of supported ultra-hard ultra-thin films and nanostructures," Sci. Rep. **9**, 4075 (2019).

[144] J. Stern, B. Terris, H. Mamin, and D. Rugar, "Deposition and imaging of localized charge on insulator surfaces using a force microscope," Appl. Phys. Lett. **53**, 2717–2719 (1988).

[145] A. Barboza, A. Gomes, B. Archanjo, P. Araujo, A. Jorio, A. Ferlauto, H. Chacham, B. Neves *et al.*, "Deformation induced semiconductor-metal transition in single wall carbon nanotubes probed by electric force microscopy," Phys. Rev. Lett. **100**, 256804 (2008).

[146] A. P. Barboza, M. J. Matos, H. Chacham, R. J. Batista, A. B. de Oliveira, M. S. Mazzoni, and B. R. Neves, "Compression-induced modification of boron nitride layers: A conductive two-dimensional bn compound," ACS Nano **12**, 5866–5872 (2018).

[147] A. P. Barboza, A. C. Souza, M. J. Matos, J. C. Brant, T. C. Barbosa, H. Chacham, M. S. Mazzoni, and B. R. Neves, "Graphene/h-BN heterostructures under pressure: From van der Waals to covalent," Carbon **155**, 108–113 (2019).

[148] A. Barboza, H. Chacham, and B. Neves, "Universal response of single-wall carbon nanotubes to radial compression," Phys. Rev. Lett. **102**, 025501 (2009).

[149] K. Watanabe, T. Taniguchi, and H. Kanda, "Direct-bandgap properties and evidence for ultraviolet lasing of hexagonal boron nitride single crystal," Nat. Mater. **3**, 404–409 (2004).

[150] F. Cellini, F. Lavini, E. Chen, A. Bongiorno, F. Popovic, R. L. Hartman, R. Dingreville, and E. Riedo, "Pressure-induced formation and mechanical properties of 2D diamond boron nitride," Adv. Sci. **8**, 2002541 (2021).

[151] Q. H. Wang, K. Kalantar-Zadeh, A. Kis, J. N. Coleman, and M. S. Strano, "Electronics and optoelectronics of two-dimensional transition metal dichalcogenides," Nat. Nanotechnol. **7**, 699–712 (2012).

[152] W. Choi, N. Choudhary, G. H. Han, J. Park, D. Akinwande, and Y. H. Lee, "Recent development of two-dimensional transition metal dichalcogenides and their applications," Mater. Today **20**, 116–130 (2017).

[153] S. Bhattacharyya and A. K. Singh, "Semiconductor-metal transition in semiconducting bilayer sheets of transition-metal dichalcogenides," Phys. Rev. B **86**, 075454 (2012).

[154] A. Kumar and P. Ahluwalia, "Electronic structure of transition metal dichalcogenides monolayers 1H-MX$_2$ (M = Mo, W; X = S, Se, Te) from ab-initio theory: New direct band gap semiconductors," Eur. Phys. J. B **85**, 1–7 (2012).

[155] X. Su, W. Ju, R. Zhang, C. Guo, Y. Yong, H. Cui, and X. Li, "Band gap modulation of transition-metal dichalcogenide MX$_2$ nanosheets by in-plane strain," Physica E **84**, 216–222 (2016).

[156] D. Fu, J. Zhou, S. Tongay, K. Liu, W. Fan, T.-J. King Liu, and J. Wu, "Mechanically modulated tunneling resistance in monolayer MoS$_2$," Appl. Phys. Lett. **103**, 183105 (2013).

[157] A. P. Nayak, S. Bhattacharyya, J. Zhu, J. Liu, X. Wu, T. Pandey, C. Jin, A. K. Singh, D. Akinwande, and J.-F. Lin, "Pressure-induced semiconducting to metallic transition in multilayered molybdenum disulphide," Nat. Commun. **5**, 1–9 (2014).

[158] Z.-H. Chi, X.-M. Zhao, H. Zhang, A. F. Goncharov, S. S. Lobanov, T. Kagayama, M. Sakata, and X.-J. Chen, "Pressure-induced metallization of molybdenum disulfide," Phys. Rev. Lett. **113**, 036802 (2014).

[159] M. V. Bessa, W. D. Freitas, N. P. Neme, L. G. Martins, A. P. Barboza, M. J. Matos, M. S. Mazzoni, and B. R. Neves, "Electromechanical modulations in transition metal dichalcogenide nanosheets: Implications for environmental sensors," ACS Appl. Nano Mater. **4**, 11305–11311 (2021).

[160] A. P. M. Barboza, H. Chacham, C. K. Oliveira, T. F. Fernandes, E. H. M. Ferreira, B. S. Archanjo, R. J. Batista, A. B. de Oliveira, and B. R. Neves, "Dynamic negative compressibility of few-layer graphene, h-BN, and MoS$_2$," Nano Lett. **12**, 2313–2317 (2012).

[161] A. B. Alencar, A. P. M. Barboza, B. S. Archanjo, H. Chacham, and B. R. Neves, "Experimental and theoretical investigations of monolayer and few-layer talc," 2D Mater. **2**, 015004 (2015).

[162] J. A. M. Meza, C. Lubin, F. Thoyer, and J. Cousty, "Tip induced mechanical deformation of epitaxial graphene grown on reconstructed 6H–SiC (0001) surface during scanning tunneling and atomic force microscopy studies," Nanotechnology **26**, 255704 (2015).

[163] M. Rejhon, F. Lavini, A. Khosravi, M. Shestopalov, J. Kunc, E. Tosatti, and E. Riedo, "Relation between interfacial shear and friction force in 2D materials," Nat. Nanotechnol. **17**, 1280–1287 (2022).

[164] M. Yankowitz, K. Watanabe, T. Taniguchi, P. San-Jose, and B. J. LeRoy, "Pressure-induced commensurate stacking of graphene on boron nitride," Nat. Commun. **7**, 13168 (2016).

[165] A. Lipatov, P. Chaudhary, Z. Guan, H. Lu, G. Li, O. Crégut, K. D. Dorkenoo, R. Proksch, S. Cherifi-Hertel, D.-F. Shao *et al.*, "Direct observation of ferroelectricity in two-dimensional MoS$_2$," npj 2D Mater. Appl. **6**, 18 (2022).

[166] A. G. Kvashnin, L. A. Chernozatonskii, B. I. Yakobson, and P. B. Sorokin, "Phase diagram of quasi-two-dimensional carbon, from graphene to diamond," Nano Lett. **14**, 676–681 (2014).

[167] C. Tantardini, A. G. Kvashnin, C. Gatti, B. I. Yakobson, and X. Gonze, "Computational modeling of 2D materials under high pressure and their chemical bonding: Silicene as possible field-effect transistor," ACS Nano **15**, 6861–6871 (2021).

[168] G. Kern, G. Kresse, and J. Hafner, "Ab initio calculation of the lattice dynamics and phase diagram of boron nitride," Phys. Rev. B **59**, 8551–8559 (1999).

[169] L. A. Chernozatonskii, P. B. Sorokin, A. G. Kvashnin, and D. G. Kvashnin, "Diamond-like c$_2$h nanolayer, diamane: Simulation of the structure and properties," JETP Lett. **90**, 134–138 (2009).

[170] Y. Takagi and K. Kusakabe, "Transition from direct band gap to indirect band gap in fluorinated carbon," Phys. Rev. B **65**, 121103 (2002).

[171] F. Piazza, K. Cruz, M. Monthioux, P. Puech, and I. Gerber, "Raman evidence for the successful synthesis of diamane," Carbon **169**, 129–133 (2020).

[172] J. M. Soler, E. Artacho, J. D. Gale, A. García, J. Junquera, P. Ordejón, and D. Sánchez-Portal, "The SIESTA method for *ab initio* order-N materials simulation," J. Phys.: Condens. Matter **14**, 2745 (2002).

[173] P. Hohenberg and W. Kohn, "Inhomogeneous electron gas," Phys. Rev. **136**, B864–B871 (1964).

[174] W. Kohn and L. J. Sham, "Self-consistent equations including exchange and correlation effects," Phys. Rev. **140**, A1133–A1138 (1965).

[175] N. Troullier and J. L. Martins, "Efficient pseudopotentials for plane-wave calculations," Phys. Rev. B **43**, 1993–2006 (1991).

[176] L. Kleinman and D. M. Bylander, "Efficacious form for model pseudopotentials," Phys. Rev. Lett. **48**, 1425–1428 (1982).

[177] Y.-P. Xie, X.-J. Zhang, and Z.-P. Liu, "Graphite to diamond: Origin for kinetics selectivity," J. Am. Chem. Soc. **139**, 2545–2548 (2017).

[178] P. Johari and V. B. Shenoy, "Tuning the electronic properties of semiconducting transition metal dichalcogenides by applying mechanical strains," ACS Nano **6**, 5449–5456 (2012).

[179] E. Scalise, M. Houssa, G. Pourtois, V. Afanas'ev, and A. Stesmans, "Strain-induced semiconductor to metal transition in the two-dimensional honeycomb structure of MoS$_2$," Nano Res. **5**, 43–48 (2012).

[180] A. Kumar and P. K. Ahluwalia, "Semiconductor to metal transition in bilayer transition metals dichalcogenides MX_2 (M = Mo, W; X = S, Se, Te)," Modell. Simul. Mater. Sci. Eng. **21**, 065015 (2013).

[181] Z. Tao, J. Du, Z. Qi, K. Ni, S. Jiang, and Y. Zhu, "Raman spectroscopy study of sp^2 to sp^3 transition in bilayer graphene under high pressures," Appl. Phys. Lett. **116**, 133101 (2020).

[182] L. A. Chernozatonskii, V. A. Demin, and D. G. Kvashnin, "Moire diamones: New diamond-like films of semifunctionalized twisted graphene layers," J. Phys. Chem. Lett. **13**, 5399–5404 (2022).

[183] M. Bykov, E. Bykova, A. V. Ponomareva, F. Tasnadi, S. Chariton, V. B. Prakapenka, K. Glazyrin, J. S. Smith, M. F. Mahmood, I. A. Abrikosov *et al.*, "Realization of an ideal Cairo tessellation in nickel diazenide NiN$_2$: High-pressure route to pentagonal 2D materials," ACS Nano **15**, 13539–13546 (2021).

[184] M. Bykov, T. Fedotenko, S. Chariton, D. Laniel, K. Glazyrin, M. Hanfland, J. S. Smith, V. B. Prakapenka, M. F. Mahmood, A. F. Goncharov *et al.*, "High-pressure synthesis of Dirac materials: Layered van der Waals bonded BeN$_4$ polymorph," Phys. Rev. Lett. **126**, 175501 (2021).

[185] Q. Song, C. A. Occhialini, E. Ergeçen, B. Ilyas, D. Amoroso, P. Barone, J. Kapeghian, K. Watanabe, T. Taniguchi, A. S. Botana *et al.*, "Evidence for a single-layer van der Waals multiferroic," Nature **602**, 601–605 (2022).

[186] Y. Tokura, S. Seki, and N. Nagaosa, "Multiferroics of spin origin," Rep. Prog. Phys. **77**, 076501 (2014).

[187] D. Zhong, K. L. Seyler, X. Linpeng, N. P. Wilson, T. Taniguchi, K. Watanabe, M. A. McGuire, K.-M. C. Fu, D. Xiao, W. Yao *et al.*, "Layer-resolved magnetic proximity effect in van der Waals heterostructures," Nat. Nanotechnol. **15**, 187–191 (2020).

[188] H. Yu, G.-B. Liu, J. Tang, X. Xu, and W. Yao, "Moiré excitons: From programmable quantum emitter arrays to spin-orbit–coupled artificial lattices," Sci. Adv. **3**, e1701696 (2017).

[189] K. Tran, G. Moody, F. Wu, X. Lu, J. Choi, K. Kim, A. Rai, D. A. Sanchez, J. Quan, A. Singh *et al.*, "Evidence for moiré excitons in van der Waals heterostructures," Nature **567**, 71–75 (2019).

[190] K. L. Seyler, P. Rivera, H. Yu, N. P. Wilson, E. L. Ray, D. G. Mandrus, J. Yan, W. Yao, and X. Xu, "Signatures of moiré-trapped valley excitons in MoSe$_2$/WSe$_2$ heterobilayers," Nature **567**, 66–70 (2019).

[191] C. Jin, E. C. Regan, A. Yan, M. I. B. Utama, D. Wang, S. Zhao, Y. Qin, S. Yang, Z. Zheng, S. Shi *et al.*, "Observation of moiré excitons in WSe$_2$/WS$_2$ heterostructure superlattices," Nature **567**, 76–80 (2019).